

Finite size scaling in Ising-like systems with quenched random fields: Evidence of hyperscaling violation

R. L. C. Vink and T. Fischer

*Institute of Theoretical Physics, Georg-August-Universität Göttingen,
Friedrich-Hund-Platz 1, D-37077 Göttingen, Germany*

K. Binder

Institut für Physik, Johannes Gutenberg-Universität, Staudinger Weg 7, D-55099 Mainz, Germany

In systems belonging to the universality class of the random field Ising model, the standard hyperscaling relation between critical exponents does not hold, but is replaced by a modified hyperscaling relation. As a result, standard formulations of finite size scaling near critical points break down. In this work, the consequences of modified hyperscaling are analyzed in detail. The most striking outcome is that the free energy cost ΔF of interface formation at the critical point is no longer a universal constant, but instead increases as a power law with system size, $\Delta F \propto L^\theta$, with θ the violation of hyperscaling critical exponent, and L the linear extension of the system. This modified behavior facilitates a number of new numerical approaches that can be used to locate critical points in random field systems from finite size simulation data. We test and confirm the new approaches on two random field systems in three dimensions, namely the random field Ising model, and the demixing transition in the Widom-Rowlinson fluid with quenched obstacles.

I. INTRODUCTION

Understanding the effects of quenched random disorder on phase transitions has been a longstanding challenge [1–6]. Analysis of experiments on such systems is typically more difficult than work on pure systems [4]. Theoretical methods are hampered by the fact that, for spin glasses and systems exposed to random fields, the marginal dimension $d^* = 6$ (the marginal dimension is the dimension above which mean field theory is believed to be reliable). In contrast, for pure systems, $d^* = 4$ [7, 8]. As a consequence, predictions of renormalization group expansions in $\epsilon = d^* - d$ dimensions tend to be less reliable in the physically relevant dimensions ($d = 2, 3$) when quenched disorder comes into play. Computer simulations, albeit very useful for the study of critical phenomena in pure systems [9–11], suffer from the problem that for systems exhibiting quenched random disorder an additional average over many samples drawn from the distribution characterizing the disorder needs to be taken. The disorder average, denoted $[\cdot]$, comes in addition to the usual thermal average, denoted $\langle \cdot \rangle$, and hence the computational effort is order of magnitudes larger. Since most analysis of critical phenomena by simulations [9–11] relies on finite size scaling [12–16], lack of self-averaging in random systems [17–20] is also a problem.

For Ising ferromagnets diluted with nonmagnetic impurities there is no doubt that the transition, from the high-temperature disordered to the low-temperature ordered phase, remains second order in $d = 2, 3$ [3]. In addition, the hyperscaling relation [7] between critical exponents remains valid

$$2 - \alpha = 2\beta + \gamma = d\nu \quad (d = 2, 3), \quad (1)$$

and rather accurate estimates for these exponents are available [21] (we use standard symbols to denote the ex-

ponents; definitions are provided in Section II). For Ising ferromagnets in random fields, however, the situation is radically different. In $d = 3$ dimensions, the existence of a transition at nonzero temperature was controversial until a proof for the existence of a spontaneous magnetization settled this issue [22]; rigorous results on the order of the phase transition in the $d = 3$ random field Ising model (RFIM) are still lacking however. If one accepts the evidence from numerical studies [23, 24] that the transition is second order, it must have very unconventional critical behavior [25–27]. The key point is that the standard hyperscaling relation, Eq. (1), no longer holds, but is replaced by

$$2 - \alpha = 2\beta + \gamma = \nu(d - \theta). \quad (2)$$

The exponent θ , called the “violation of hyperscaling exponent”, is believed to be [28–30]

$$\theta = \gamma/\nu = 2 - \eta, \quad (3)$$

where the critical exponent η describes the decay of the spin pair correlation function right at the critical temperature [7]. In addition, it is believed [25–27] that critical slowing down in the RFIM is not described by the usual power law for the relaxation time $\tau \propto \xi^z$, with z the “dynamic critical exponent” [31] and ξ the correlation length, but instead is governed by a much more severe “thermally activated critical slowing down” [25–27]

$$\ln \tau \propto \xi^\theta, \quad (4)$$

with $T \rightarrow T_c$ from above. It should not come as a surprise that Eqs. (2), (3) and (4) make the study of the RFIM by Monte Carlo (MC) methods very difficult, and early studies even claimed a weak first order transition [32]. Another problem is that standard finite size scaling formulations typically rely on the validity of hyperscaling, which does not hold in the RFIM [9, 14]. Some of

the consequences resulting from the violation of hyperscaling, Eq. (2), were already noted in previous works [33], and exploited in recent studies of colloid-polymer demixing in random porous media [6].

The purpose of the present paper is to analyze the consequences of Eq. (2) for finite size scaling in more detail. In particular, we shall focus on the free energy barrier ΔF_L separating the coexisting phases for $T \leq T_c$ in a finite system of linear extension L . It has been found that ΔF_L increases quite strongly with L at $T = T_c$ in the RFIM [35]. This behavior is puzzling because a growing barrier is usually associated with a first-order phase transition. In this work, the theoretical justification for this behavior is provided. We will show that the barrier, which in the regime where the transition is first-order scales as

$$\Delta F_L = 2f_{\text{int}}L^{d-1} \quad (T < T_c), \quad (5)$$

with f_{int} the interfacial tension [15], right at the critical point is related to the hyperscaling violation critical exponent

$$\Delta F_L \propto L^\theta \quad (T = T_c). \quad (6)$$

The factor-of-two in Eq. (5) is a consequence of periodic boundary conditions, which induce two interfaces in the system when $T < T_c$. We will provide numerical evidence in favor of Eq. (6) using simulation results obtained for two random field systems in $d = 3$ dimensions, namely the RFIM and the Widom-Rowlinson fluid with quenched obstacles. We emphasize that in $d = 2$ dimensions the RFIM is without a phase transition, in which case the analysis of the present paper does not apply.

II. THEORETICAL BACKGROUND

We consider a system of N Ising spins, situated on a d -dimensional lattice of linear extension L with periodic boundaries, inside an external magnetic field H . The instantaneous magnetization per spin is defined as

$$m = \frac{1}{N} \sum_{i=1}^N S_i, \quad N = L^d, \quad (7)$$

with $S_i = \pm 1$ the value of the spin at the i -th lattice site. We assume that the system, in the thermodynamic limit $L \rightarrow \infty$, undergoes a second-order phase transition at critical temperature $T = T_c$ and field $H = H_c$. Following standard practice, we introduce the relative deviations

$$t \equiv T/T_c - 1, \quad h \equiv H/H_c - 1. \quad (8)$$

In the vicinity of the critical point ($t = 0, h = 0$), the specific heat C , susceptibility χ , and correlation length ξ diverge as power laws

$$\begin{aligned} C(t, h = 0) &\propto |t|^{-\alpha}, & \chi(t, h = 0) &\propto |t|^{-\gamma}, \\ \xi(t, h = 0) &\propto |t|^{-\nu}. \end{aligned} \quad (9)$$

In the ordered phase $T < T_c$, a finite magnetization M (order parameter) and interfacial tension f_{int} develop

$$\begin{aligned} M(t, h = 0) &\propto |t|^\beta \quad (t < 0), \\ f_{\text{int}}(t, h = 0) &\propto |t|^\mu \quad (t < 0). \end{aligned} \quad (10)$$

We first give a heuristic derivation of the standard hyperscaling relation, Eq. (1), which is valid in pure systems, i.e. without quenched random fields. Following the static scaling hypothesis [34], the singular part of the free energy density takes the form

$$f_{\text{sing}}(t, h) = |t|^{2-\alpha} \tilde{f}(h/|t|^{\beta+\gamma}), \quad (11)$$

with $\tilde{f}(x)$ a scaling function. The order parameter is obtained by differentiating f_{sing} once with respect to the external field

$$M(t, h = 0) \propto \left. \frac{\partial f_{\text{sing}}}{\partial h} \right|_{h=0} \propto |t|^{2-\alpha-\beta-\gamma}, \quad (12)$$

which, upon comparing to Eq. (10), immediately yields $2 - \alpha = 2\beta + \gamma$ [34]. Near criticality, the singular part of the free energy can be attributed to correlated regions of spins (clusters) of linear dimension ξ [7, 34]. Each cluster has essentially one Ising degree of freedom (magnetization direction up or down), and can orient independently from its neighbors. Thus, while at $T \rightarrow \infty$ the total free energy F of the system is due to the entropy of N non-interacting spins, $F = -(k_B T \ln 2)N$, near T_c we can attribute the singular part of F to the entropy of N/ξ^d independent clusters of spins, $F = -(k_B T \ln 2)N/\xi^d$, and hence

$$f_{\text{sing}}(t, 0) \propto \xi^{-d} \propto |t|^{d\nu}, \quad (13)$$

where in the last step Eq. (9) was used. Comparing the above equation to Eq. (11), the standard hyperscaling relation $2 - \alpha = d\nu$ immediately follows.

For an Ising system in quenched random fields near criticality the situation is different. To be specific, consider a random field $\pm r$ acting on each spin (with the signs \pm drawn with equal probability such that $\langle r \rangle = 0$). We can still split the system into clusters of linear dimension ξ , such that each cluster may be considered as independent from its neighbors. However, the main contribution to f_{sing} in this case is not the entropy, Eq. (13), but rather the Zeeman energy due to the coupling to the random field. In a region of volume ξ^d , the sum of the random fields exhibits Poissonian fluctuations $\pm r \xi^{d/2}$. The random field excess per spin is therefore of order

$$\Delta_R \propto \pm r \xi^{-d/2}, \quad (14)$$

which may be conceived as an external field acting on the spins in the region. This implies a finite magnetization per spin

$$\langle m \rangle \propto \chi \Delta_R \propto \pm r \chi \xi^{-d/2}, \quad (15)$$

with χ the susceptibility. The Zeeman contribution to the free energy thus becomes

$$f_{\text{sing}}(t, 0) \propto \langle m \rangle \Delta_R \propto r^2 \chi \xi^{-d} \propto |t|^{d\nu-\gamma}, \quad (16)$$

which dominates the entropy contribution, Eq. (13), upon approach of the critical point $t \rightarrow 0$. If we insist that f_{sing} retains the scaling form of Eq. (11), it follows that $2 - \alpha = d\nu - \gamma$; using $\theta = \gamma/\nu$ (Eq. (3)) then yields the modified hyperscaling relation (Eq. (2)).

Next, we consider the exponent μ of the interfacial tension (Eq. (10)). Since Eq. (11) is a free energy per volume, and since near T_c the correlation length is the only relevant length scale, a simple dimensional argument implies that

$$f_{\text{int}} \propto f_{\text{sing}} \xi \rightarrow \mu = 2 - \alpha - \nu. \quad (17)$$

In case of hyperscaling this implies $\mu = (d - 1)\nu$. The important point of the present discussion is that this relation does not hold in the RFIM, since the hyperscaling relation, Eq. (1), is violated and replaced by the modified relation, Eq. (2). We can still infer that Eq. (17) should hold, but now one must use Eq. (2), which leads to $\mu_{\text{RFIM}} = (d - 1 - \theta)\nu$. Finally, we discuss fluctuations, which are typically large near phase transitions. In the pure Ising model, the thermally averaged magnetization plays the role of order parameter M , while the susceptibility χ reflects its thermal fluctuations

$$\text{pure Ising model} \rightarrow \begin{cases} M = \langle |m| \rangle, \\ \chi = L^d (\langle m^2 \rangle - \langle |m| \rangle^2). \end{cases} \quad (18)$$

For the RFIM, the obvious generalizations are

$$\text{RFIM} \rightarrow \begin{cases} M = [\langle |m| \rangle], \\ \chi_{\text{con}} = L^d [\langle m^2 \rangle - \langle |m| \rangle^2], \end{cases} \quad (19)$$

with $[\cdot]$ the disorder average (factors of $k_B T$ have been dropped in our definitions). χ and χ_{con} are called ‘‘connected’’ susceptibilities: they reflect thermal fluctuations, which are present in both models, and diverge at criticality with exponent γ (Eq. (9)). Note that our definitions of the order parameter and susceptibilities use the absolute value of the instantaneous magnetization, as is commonly done in simulations [36].

In the RFIM, we can also define a ‘‘disconnected’’ susceptibility [27]

$$\text{RFIM} \rightarrow \chi_{\text{dis}} \equiv L^d ([\langle |m| \rangle^2] - [\langle |m| \rangle]^2), \quad (20)$$

which does not have its analogue in the pure model (removing the disorder average $[\cdot]$ trivially yields $\chi_{\text{dis}} = 0$). The motivation to introduce χ_{dis} stems from the observation that $\langle |m| \rangle$ depends on the random field sample. Hence, in the disorder average, there will be sample-to-sample fluctuations in $\langle |m| \rangle$, which is precisely what χ_{dis} corresponds to. Upon approach of the critical point, the disconnected susceptibility also diverges

$$\chi_{\text{dis}} \propto |t|^{\bar{\gamma}}, \quad (21)$$

TABLE I. Critical exponents of the pure Ising model and RFIM in $d = 3$ dimensions; see Ref. [27] for a more elaborate list of results for the RFIM.

	pure Ising	RFIM
β	0.326 [8]	0.0–0.02 [37] 0.06 [24] 0 [23]
ν	0.630 [8]	1.14 [37], 1.67 [37] 1.02 [24] 1.1 [23] 2.25 [38]
γ	1.240 [8]	1.9 [24]
$\bar{\gamma}$	–	3.4–5.0 [37]
	–	2.9 [24]

defining a new critical exponent $\bar{\gamma}$. It is predicted that $\bar{\gamma} = 2\gamma$ [25–30], implying that sample-to-sample fluctuations dominate over thermal ones at criticality. If we substitute, in Eq. (2), $\theta \rightarrow \gamma/\nu$ and $\gamma \rightarrow \bar{\gamma}/2$, the modified hyperscaling relation becomes

$$2\beta + \bar{\gamma} = d\nu, \quad (22)$$

which is just the standard hyperscaling relation, Eq. (1), but with γ replaced by $\bar{\gamma}$.

III. FINITE SIZE SCALING

A. pure Ising model

We first consider finite-size scaling (FSS) in the pure Ising model in $d = 3$ dimensions. The Hamiltonian is given by

$$\mathcal{H}_{\text{Ising}} = -J \sum_{\langle i, j \rangle} S_i S_j - H \sum_i S_i, \quad J > 0, \quad (23)$$

with $\langle i, j \rangle$ a sum over nearest neighbors. In what follows, the temperature T is expressed in units of k_B/J , with k_B the Boltzmann constant. For the $d = 3$ Ising model on cubic periodic lattices, the critical temperature $T_c \approx 4.511$ [36]. The critical exponents are known relatively precisely, although not exactly (Table I).

A key quantity in the numerical study of phase transitions is the order parameter distribution (OPD), denoted $P_L(m)$, and defined as the probability to observe the system in a state with magnetization m . We assume the OPD is normalized: $\int_{-1}^{+1} P_L(m) dm = 1$. The OPD depends on the system size L , and on the control parameters T and H . In the pure Ising model, due to spin reversal symmetry, the critical field $H_c = 0$, and so we set the external field to zero. The OPD is then an even function, $P_L(-m) = P_L(m)$, irrespective of T and L .

In the ordered phase, $T < T_c$, the transition is first-order. There exists a spontaneous magnetization, which

may be positive or negative. The OPD is a superposition of two Gaussians, centered around $m = \pm m_0$, with exponentially small finite size effects in the peak positions [39]. The definition $M = \langle |m| \rangle$ corresponds to (half) the peak-to-peak distance. In the disordered phase, $T > T_c$, the OPD tends to a single Gaussian peak centered around $m = 0$. In both cases, the system self-averages: the peak widths decay $\propto L^{-d/2}$, ultimately becoming sharp δ -functions.

At criticality, the L -dependence of the OPD is given by the scaling form [14, 40]

$$P_L(m) \propto \tilde{P}(L^b m) \rightarrow \langle m^k \rangle \propto L^{-kb} \quad (T = T_c) \quad (24)$$

with b a constant, and $\tilde{P}(x)$ a scaling function characteristic of the Ising universality class. The standard FSS expressions for the order parameter and susceptibility are [12–14]

$$M \propto L^{-\beta/\nu}, \quad \chi \propto L^{\gamma/\nu} \quad (T = T_c). \quad (25)$$

In order to be consistent with these expressions, Eq. (24) requires $b = \beta/\nu$, and the validity of standard hyperscaling. For the pure Ising model, the OPD at criticality is bimodal with overlapping peaks (Fig. 1(a)). If one plots the distributions versus the scaling variable, $x = L^{\beta/\nu} m$, the curves for different L overlap (Fig. 1(b)). A further consequence of Eq. (24) is that cumulant ratios such as

$$U_1 \equiv \langle m^2 \rangle / \langle |m| \rangle^2, \quad U_4 \equiv \langle m^4 \rangle / \langle m^2 \rangle^2, \quad \text{etc.}, \quad (26)$$

are L -independent at criticality. Since the peaks in the critical OPD of the pure Ising model overlap (as opposed to being sharp), the corresponding cumulant ratios are distinctly different from the off-critical values. For example, considering the U_1 cumulant, it holds that

$$\lim_{L \rightarrow \infty} U_1 = \begin{cases} 1 & T < T_c, \\ U_1^* & T = T_c, \\ \pi/2 & T > T_c, \end{cases} \quad (27)$$

where $U_1^* = 1.2391(14)$ for the $d = 3$ Ising model [41]. This behavior is extremely useful to extract T_c from simulation data [9–11, 14], see Fig. 1(c). Note that U_1 is essentially the ratio between the order parameter and its thermal fluctuations

$$\sigma_T^2 \equiv \frac{\langle m^2 \rangle - \langle |m| \rangle^2}{\langle |m| \rangle^2} = U_1 - 1. \quad (28)$$

The fact that $U_1 = U_1^*$ at criticality implies that σ_T remains finite. Put differently: the thermal fluctuations of the order parameter M remain comparable to M itself at T_c . From this consideration one also understands why the peaks in the OPD are broad and overlapping. Alternatively, we may write

$$\sigma_T^2 = \chi / L^d M^2, \quad (29)$$

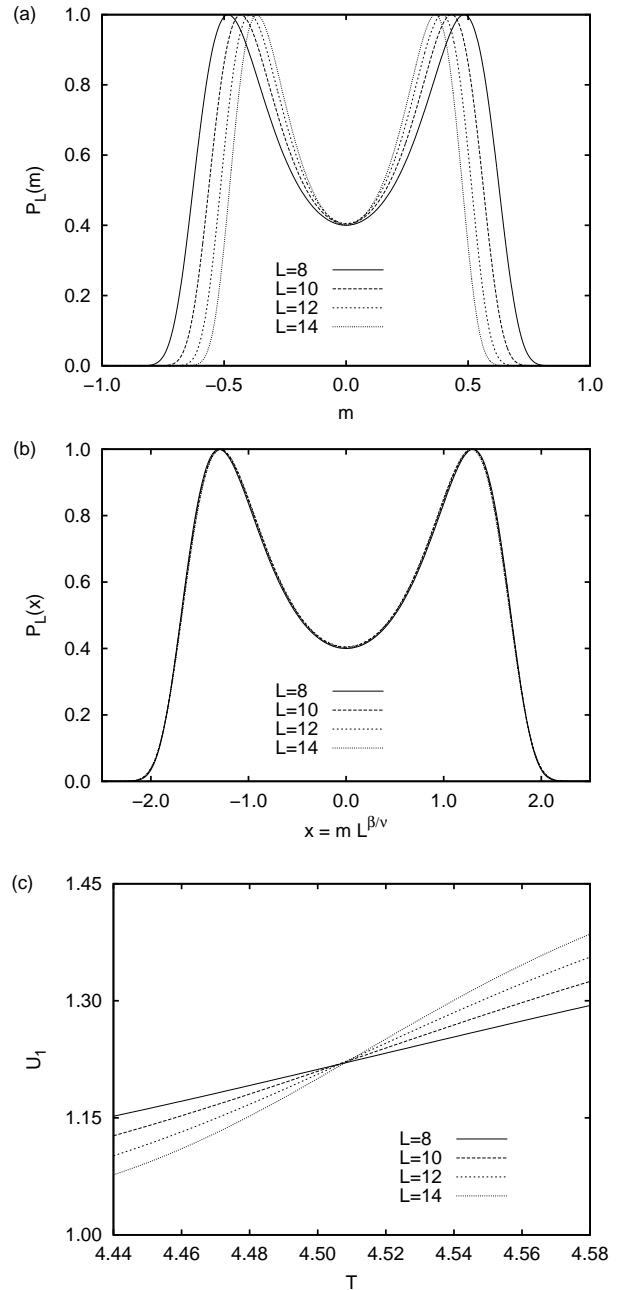


FIG. 1. FSS in the $d = 3$ pure Ising model in the critical regime. The linear dimension L is given in units of the lattice spacing. (a) OPD $P_L(m)$ obtained at $T = T_c$, $H = H_c = 0$, and for several system sizes. (b) The same data plotted versus the scaling variable, with the critical exponents taken from Table I; the data for different L overlap. (c) Demonstration of the cumulant intersection method to locate T_c . Plotted is U_1 versus T for several system sizes. At the critical point, the curves for different L intersect. In the ordered (disordered) phase, $U_1 \rightarrow 1$ ($U_1 \rightarrow \pi/2$) as L increases, in accord with Eq. (27).

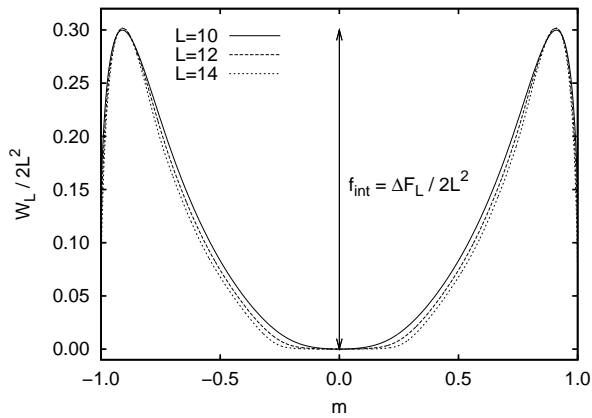


FIG. 2. Finite size effects in the $d = 3$ pure Ising model in the ordered phase, where the transition is first-order. Plotted is the scaled-and-shifted logarithm of the OPD, $W_L = \ln P_L(m)$, for various system sizes at $T = 3.33$, which is well below T_c . The peak height corresponds to the interfacial tension f_{int} . Note also the flat region unfolding between the peaks as L increases.

from which, using Eq. (25) and hyperscaling, one also immediately derives that σ_T is L -independent at criticality.

The free energy barrier is obtained from the logarithm of the OPD $W_L = \ln P_L(m)$. We define ΔF_L as the average peak height, measured from the minimum “in-between” the peaks. In the ordered phase, $T < T_c$, the transition is first-order, and the barrier is related to the interfacial tension f_{int} via Eq. (5). This is shown in Fig. 2. Note also that the peak positions – at least on the scale of the graph – do not reveal any strong L dependence either, consistent with exponentially small finite size effects [39]. The peaks also become sharper as L increases, showing that the system is self-averaging. Finally, we note that a flat region between the peaks in W_L unfolds as L increases. This is a sign that interactions between the interfaces through the periodic boundaries are vanishing [42].

Precisely at criticality, the scaling of the barrier is different. We may still assume that Eq. (5) holds, but on a length scale that is set by the correlation length

$$\Delta F_\xi \propto f_{\text{int}} \xi^{d-1} \propto \xi^{d-1-(2-\alpha-\nu)/\nu}, \quad (30)$$

where in the last step the critical power law of f_{int} and Eq. (17) were used; by virtue of hyperscaling, the length scale drops out. Hence, the barrier is a constant L -independent value $\Delta F_L \equiv \Delta F^*$ at criticality. Of course, the fact that the OPD at $T = T_c$ has a universal shape, see Fig. 1(b), also implies this property. In the pure Ising model, the barrier thus scales as

$$\lim_{L \rightarrow \infty} \Delta F_L = \begin{cases} 2f_{\text{int}} L^{d-1} & T < T_c, \\ \Delta F^* & T = T_c, \\ 0 & T > T_c. \end{cases} \quad (31)$$

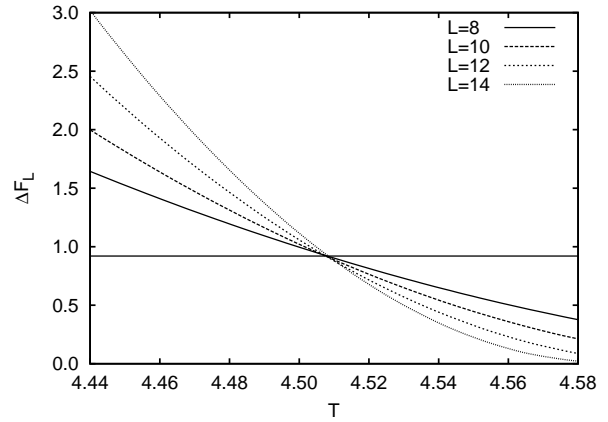


FIG. 3. Scaling of the free energy barrier ΔF_L in the pure Ising model. By plotting ΔF_L versus T for various L , the critical temperature appears as an intersection point. The horizontal line marks the (universal) value $\Delta F^* \sim 0.9$ for the $d = 3$ Ising model.

This behavior is also well-suited to locate T_c [43]. For instance, one plots ΔF_L versus T for various L ; at the critical point, the data for different system sizes intersect (Fig. 3).

In brief, we have summarized FSS in the pure Ising model. The important message is that, due to hyperscaling, the OPD assumes a universal shape at the critical point. As a result, the free energy barrier and selected cumulant ratios assume non-trivial L -independent values, which can be used to locate the critical point. We also note that, by using the intersection methods of U_1 and ΔF_L (Fig. 1(c) and Fig. 3), moderate system sizes suffice to locate the critical point with an accuracy better than one part in a thousand.

B. RFIM

We now consider FSS in the RFIM at its critical point. The Hamiltonian reads as

$$\mathcal{H}_{\text{RFIM}} = -J \sum_{\langle i,j \rangle} S_i S_j - \sum_i r_i S_i - H \sum_i S_i, \quad (32)$$

$J > 0$, with r_i the quenched random field acting on the spin at the i -th lattice site. It is convenient to draw r_i from a distribution that is symmetric about zero; this ensures that $H_c = 0$. The most common choices are the bimodal distribution $P(r_i) \propto \delta(r_i - \sigma) + \delta(r_i + \sigma)$ and the Gaussian $P(r_i) \propto \exp(-r_i^2/2\sigma^2)$, where σ is the random field strength. In contrast to the pure Ising model, the critical exponents of the RFIM are not known very precisely, see Table I, where several exponent estimates from theoretical and simulational works are listed. We believe it is safe to conclude that β is close to zero. Modified hyperscaling then implies $\theta = \gamma/\nu \approx 1.5$ and $\bar{\gamma}/\nu \approx 3$, where dimensionality $d = 3$ is assumed.

1. Consequences of modified hyperscaling

One of the most striking consequences of hyperscaling violation is that the thermal fluctuations become negligible at the critical point. For the RFIM, the analogue of Eq. (29) becomes $\sigma_T^2 = \chi_{\text{con}}/L^d M^2$; using the FSS expressions $M \propto L^{-\beta/\nu}$ and $\chi_{\text{con}} \propto L^{\gamma/\nu}$, it follows that

$$\sigma_T^2 \propto L^{2\beta/\nu + \gamma/\nu - d} \propto L^{-\gamma/\nu} \quad (T = T_c), \quad (33)$$

where now the modified hyperscaling relation, Eq. (2), was used. In the RFIM, σ_T thus decays to zero with increasing L , whereas in the pure Ising model σ_T saturates at a finite L -independent value.

Even though the thermal fluctuations vanish in the RFIM for large L , we must not forget about the sample-to-sample fluctuations, which are characterized by χ_{dis} . In line with σ_T , we compare the order parameter to the magnitude of sample-to-sample fluctuations as

$$\sigma_D^2 \equiv \frac{\chi_{\text{dis}}}{L^d M^2} \propto L^{2\beta/\nu + \bar{\gamma}/\nu - d} \quad (T = T_c), \quad (34)$$

where also the FSS expression $\chi_{\text{dis}} \propto L^{\bar{\gamma}/\nu}$ was used. The remarkable consequence of modified hyperscaling, Eq. (22), is therefore that $\sigma_D \propto L^0$, i.e. becoming constant at criticality. Hence, in the RFIM, it is the sample-to-sample fluctuations that “scale with L ”, not the thermal fluctuations.

How does this modified scaling affect the OPD? First note that, in addition to T , L , and H , the probability to observe a certain instantaneous magnetization m also depends on the random field sample. We therefore write $P_{L,i}(m)$, where the index i denotes one particular sample of random fields. We thus have a set of distributions. In practice, this requires that $P_{L,i}(m)$ be measured for at least $i = 1, \dots, K$ samples, where K must be large enough. We can immediately rule out that $P_{L,i}(m)$ at criticality obeys the scaling form, Eq. (24), since hyperscaling is violated. Assuming that the majority of distributions $P_{L,i}(m)$ remains bimodal at T_c – which needs to be verified in practice – the peak-to-peak distance scales as the order parameter M , while the squared peak widths $W^2 \propto \chi_{\text{con}}/L^d$. Since $\sigma_T (= W/M)$ decays to zero, see Eq. (33), it follows that the peaks in $P_{L,i}(m)$ become sharp. Again, this is in contrast to the pure Ising model, where the critical OPD features broad and overlapping peaks. In the RFIM, the shape of $P_{L,i}(m)$ at $T = T_c$ and $T < T_c$ is the same: bimodal with sharp non-overlapping peaks. The crucial difference is that, at $T = T_c$, the peak-to-peak distance decays $\propto L^{-\beta/\nu}$, while for $T < T_c$ the peak positions saturate at finite values $\pm m_0$. In the disordered phase, $T > T_c$, $P_{L,i}(m)$ should again be single peaked. As a consequence, ratios of *connected* quenched-averaged moments, such as $[\langle m^{2k} \rangle]/[\langle m^k \rangle^2]$ or $[\langle m^{2k} \rangle]/[\langle m^k \rangle]^2$, no longer assume “special” values at criticality, but equal those of the ordered phase $T < T_c$.

For instance:

$$\lim_{L \rightarrow \infty} U_{1,\text{con}} \equiv \frac{[\langle m^2 \rangle]}{[\langle m \rangle]^2} = \begin{cases} 1 & T < T_c, \\ 1 & T = T_c, \\ \pi/2 & T > T_c, \end{cases} \quad (35)$$

which does not lend itself well to extract T_c from finite-size simulation data.

Does this imply there is no “scaling” at all in the RFIM at its critical point? The answer to this question is an unequivocal “No”! Scale invariant distributions and observables still exist in the RFIM, but they must be constructed keeping modified hyperscaling, Eq. (22), in mind. For instance, to each random field sample i there corresponds a distribution $P_{L,i}(m)$, from which an average magnetization $\langle |m| \rangle_i$ can be obtained. Due to sample-to-sample fluctuations, the values $\langle |m| \rangle_i$ will generally differ. Hence, it is useful to consider the distribution $\mathcal{P}_L(\langle |m| \rangle)$, defined as the probability of a particular random field sample yielding a thermally averaged magnetization $\langle |m| \rangle$. In the absence of quenched disorder, $\mathcal{P}_L(\langle |m| \rangle)$ reduces to a δ -function; in the presence of quenched disorder, $\mathcal{P}_L(\langle |m| \rangle)$ may retain a finite width. The moments of $\mathcal{P}_L(\langle |m| \rangle)$ correspond to $[\langle |m| \rangle^k]$, which are precisely the quantities needed to compute the order parameter and the disconnected susceptibility. If we compare the average of $\mathcal{P}_L(\langle |m| \rangle)$ to its root-mean-square width, we recover σ_D of Eq. (34); by virtue of modified hyperscaling, the latter becomes constant at criticality. Hence, in the RFIM, it is the distribution $\mathcal{P}_L(\langle |m| \rangle)$ that remains broad at criticality. Our “Ansatz” is therefore that the scaling of the OPD in the pure Ising model, is replaced by scaling of $\mathcal{P}_L(\langle |m| \rangle)$ in the RFIM. We thus propose

$$\boxed{\begin{aligned} \mathcal{P}_L(\langle |m| \rangle) &\propto \tilde{\mathcal{P}}(L^b \langle |m| \rangle) \rightarrow \\ [\langle |m| \rangle^k] &\propto L^{-kb} \quad (T = T_c, \text{ RFIM}) \end{aligned}} \quad (36)$$

as the analogue of Eq. (24), with $\tilde{\mathcal{P}}(x)$ a scaling function characteristic of the RFIM. Consistency of Eq. (36) with $M \propto L^{-\beta/\nu}$ and $\chi_{\text{dis}} \propto L^{\bar{\gamma}/\nu}$ requires $b = \beta/\nu$, and the validity of modified hyperscaling, Eq. (22). Note that Eq. (36) also implies that “disconnected” cumulants such as

$$U_{1,\text{dis}} \equiv [\langle |m| \rangle^2]/[\langle |m| \rangle]^2, \quad (37)$$

become L -independent at T_c . This property suggests that a generalization of the “cumulant intersection method”, Fig. 1(c), is also feasible in the RFIM. In this case, one should plot $U_{1,\text{dis}}$ versus T ; curves for different L should intersect at T_c .

The second main consequence of modified hyperscaling concerns the scaling of the free energy barrier. The barrier is no longer constant at T_c , but rather $\Delta F_L \propto L^\theta$, with $\theta = \gamma/\nu$ the “violation of hyperscaling” exponent. This follows immediately from Eq. (30), where now the modified hyperscaling relation must be used, as well as

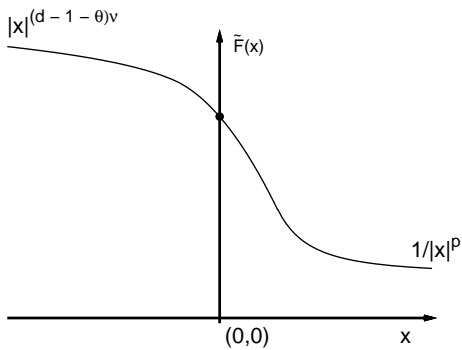


FIG. 4. Schematic plot of the scaling function $\tilde{F}(x)$, defined by Eq. (39), describing the free energy barrier ΔF_L in the RFIM versus the scaling variable $x = tL^{1/\nu}$. There occurs a smooth crossover from $\tilde{F}(x) \propto |x|^{(d-1-\theta)\nu}$ for $x \ll 0$, to $\tilde{F}(x) \propto 1/|x|^p$ for $x \gg 0$ (with $p > \nu\theta$).

the FSS “Ansatz” $\xi \propto L$ [12–14]. We thus expect, for random field Ising universality,

$$\lim_{L \rightarrow \infty} \Delta F_L \propto \begin{cases} f_{\text{int}} L^{d-1} & T < T_c, \\ L^\theta & T = T_c, \\ 0 & T > T_c. \end{cases} \quad (38)$$

Following standard FSS practice [12–14], we may also write

$$\Delta F_L = L^\theta \tilde{F}(x), \quad x = tL^{1/\nu}, \quad (39)$$

with $\tilde{F}(x)$ a scaling function. The scaling of the barrier in the ordered phase, $T < T_c$, implies that $\tilde{F}(x) \propto |x|^{(d-1-\theta)\nu}$ ($x \ll 0$). Precisely at criticality $x = 0$, we should recover Eq. (6), i.e. $\tilde{F}(0) > 0$, while in the disordered phase $T > T_c$ the barrier should vanish $\tilde{F}(x) \propto 1/|x|^p$, $p > \nu\theta$ ($x \gg 0$). From these considerations, as well as from the fact that the scaling function must be smooth, we derive the sketch shown in Fig. 4. The fact that $\tilde{F}(x)$ is a smooth function, implies that (huge) free energy barriers $\Delta F_L \propto \xi^\theta$ persist above T_c also (in sharp contrast to the pure Ising model). The latter give rise to the Arrhenius law for the relaxation time, Eq. (4).

2. Practical considerations: tuning the external field

In FSS studies, the critical region is “scanned” by varying the control parameters T and H . Mathematically, this can be conceived as following a path in the (T, H) plane. One may choose the path freely, as long as it passes through the critical point (T_c, H_c) in the thermodynamic limit. In the pure Ising model and RFIM, the critical field $H_c = 0$, and so the critical region may be scanned by varying T at fixed $H = 0$. We call this the symmetry path $l_S : H = 0$. It may also happen that H_c

is not known beforehand. This is often the case in fluids, where the analogue of H is the chemical potential. In these situations, different paths must be constructed. One example is the “equal-weight” path [44], whereby H is tuned such that the peaks in the OPD have equal area. The field now becomes a non-trivial function of temperature and system size $H = f(T, L)$. As it turns out, an infinite number of paths can be constructed along these lines [45]. Here, we will mostly use the path l_Γ , whereby H is tuned such that

$$l_\Gamma : \partial \langle m \rangle / \partial H \rightarrow \max. \quad (40)$$

Note that, when l_Γ is used in conjunction with quenched disorder, H not only depends on T and L , but also on the random field sample i , that is $H = f_i(T, L)$ with $i = 1, \dots, K$. For fixed T and L , each sample thus yields its own field H_i . A sharp transition requires that, for $T \leq T_c$, the variance of H_i vanishes as $[H^2] - [H]^2 \propto 1/L^d$, with $[H^p] = (1/K) \sum_{i=1}^K H_i^p$. It is important that the variance decays with exponent d , i.e. there should be no critical exponent involved. The field H_i that maximizes Γ is just chosen to cancel the random field excess Δ_R of Eq. (14), the square of which scales inversely with the volume. The behavior of the variance above T_c is less relevant because here we no longer have phase coexistence, and so the OPD tends to a single Gaussian peak as $L \rightarrow \infty$. The path l_Γ , as well as the “equal-weight” path, then become meaningless anyway.

IV. NUMERICAL TESTS FOR THE RFIM

We consider the RFIM Hamiltonian of Eq. (32), using Gaussian random fields with $\sigma = 1.4$, for which Newman and Barkema (NB) report as critical temperature $T_c^{\text{NB}} \approx 3.6$ [24]. Since the distribution of random fields is symmetric about zero, it also holds that $H_c = 0$. The implications of modified hyperscaling will now be verified.

A. FSS using the symmetry path l_S

We first use the symmetry path. That is, we measure $P_{L,i}(m)$ at fixed $H = 0$. Even though the critical field $H_c = 0$, spin reversal symmetry is broken in single samples, and so we do not expect $P_{L,i}(m)$ to be symmetric (only after the disorder average $[\cdot]$ has been taken is the symmetry restored). To verify that symmetric distributions are rare, we consider the ratio $A = \int_{-1}^0 P_{L,i}(m) dm / \int_{-1}^1 P_{L,i}(m) dm$. For a perfectly symmetric distribution $A = 1/2$ (the reverse is not necessarily true). Fig. 5(a) shows histograms of observed A values, measured at $T = T_c^{\text{NB}}$, and for various L . For each system size, $K \sim 10,000$ random field samples were used; more details regarding this choice are provided in

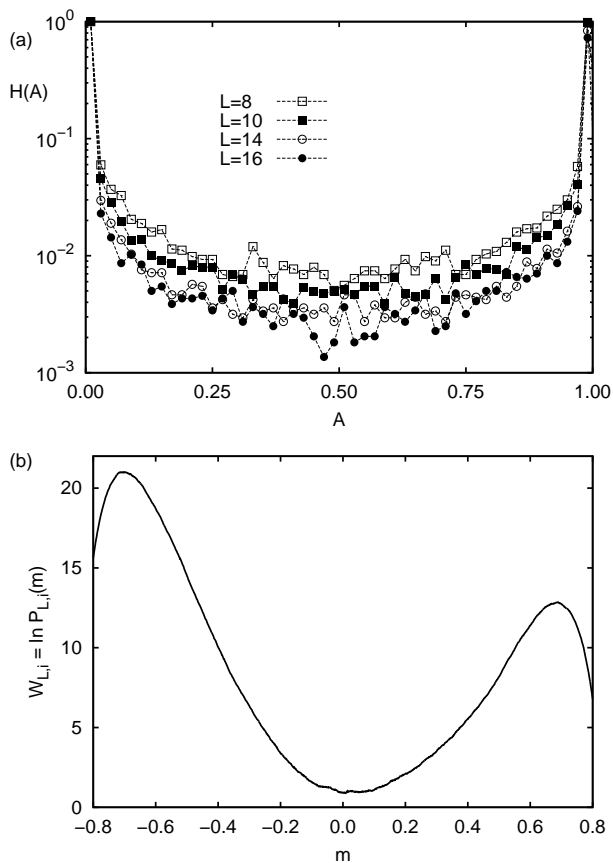


FIG. 5. Investigation of the “typical” shape of $P_{L,i}(m)$ in the RFIM at $T = T_c^{\text{NB}}$ using the symmetry path l_S . (a) Histograms $H(A)$ for various system sizes L . Note the logarithmic vertical scale. (b) Typical distribution $W_{L,i} = \ln P_{L,i}(m)$ for $L = 14$; for this distribution $A \sim 1$.

the Appendix. It is clear that symmetric distributions are rare. Most distributions yield a value of A close to zero or unity, meaning that the “weight” is entirely concentrated left or right of $m = 0$. Fig. 5(b) shows the logarithm $W_{L,i} = \ln P_{L,i}(m)$ of one such “typical” distribution. A bimodal structure is revealed, but the peak heights are very different. If one plots $P_{L,i}(m)$ itself it is clear that only a single peak survives. We conclude: by using the symmetry path, $P_{L,i}(m)$ is mostly a single peak. However, note that $H(A = 1/2)$ is not zero: distributions whose “weight” is spread symmetrically around $m = 0$ do occasionally occur. We return to this point later.

The symmetry path l_S does not lend itself well to measure free energy barriers, most distributions being single-peaked, but we can still probe sample-to-sample fluctuations¹. For each random field sample i , we calcu-

¹ A “work-around” to extract the barrier using the symmetry path can still be defined, see Appendix 4.

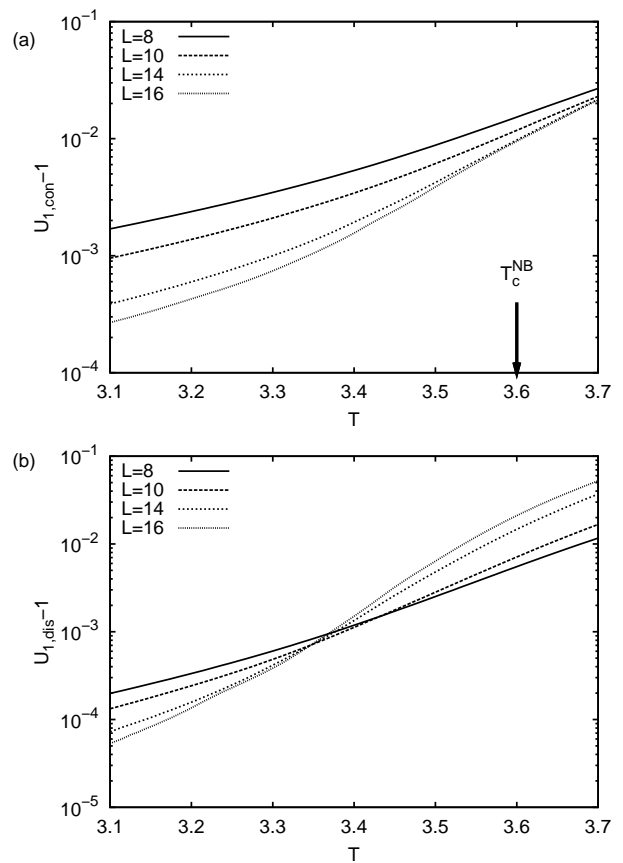


FIG. 6. Cumulant analysis of the RFIM using the symmetry path l_S . For clarity, the curves are shifted by unity, and a logarithmic vertical scale is used. (a) $U_{1,\text{con}}$ versus T for various L ; the arrow marks T_c^{NB} . (b) The disconnected cumulant $U_{1,\text{dis}}$ versus T for various L . Note the absence of intersections in $U_{1,\text{con}}$, and their presence in $U_{1,\text{dis}}$. This is conform the modified hyperscaling scenario.

late the magnetization $\langle |m| \rangle_i = \int_{-1}^{+1} |m| P_{L,i}(m) dm$, and the second moment $\langle m^2 \rangle_i = \int_{-1}^{+1} m^2 P_{L,i}(m) dm$, which are then averaged to obtain $[\langle |m| \rangle] = (1/K) \sum_{i=1}^K \langle |m| \rangle_i$, and so forth. In Fig. 6(a), we plot the connected cumulant $U_{1,\text{con}}$ (Eq. (35)) versus T for various system sizes, while (b) shows the disconnected cumulant $U_{1,\text{dis}}$, Eq. (37). The striking result is that $U_{1,\text{dis}}$ reveals an intersection point, while $U_{1,\text{RFIM}}$ does not: exactly what is predicted by modified hyperscaling! From the intersections in $U_{1,\text{dis}}$, we conclude that the critical temperature is somewhat below T_c^{NB} . Above T_c , the connected cumulant $U_{1,\text{con}} \rightarrow \pi/2$ as $L \rightarrow \infty$. If one plots $U_{1,\text{con}}$ versus T for two values of L , an intersection will also be found, at some value $T_L > T_c$; see for instance the curves for $L = 14$ and $L = 16$ in Fig. 6(a). As L increases, T_L will shift toward T_c , but there is no intersection of $U_{1,\text{con}}$ at T_c .

We still discuss the quenched-averaged distribution $Q_L(m) \equiv (1/K) \sum_{i=1}^K P_{L,i}(m)$, i.e. the arithmetic mean

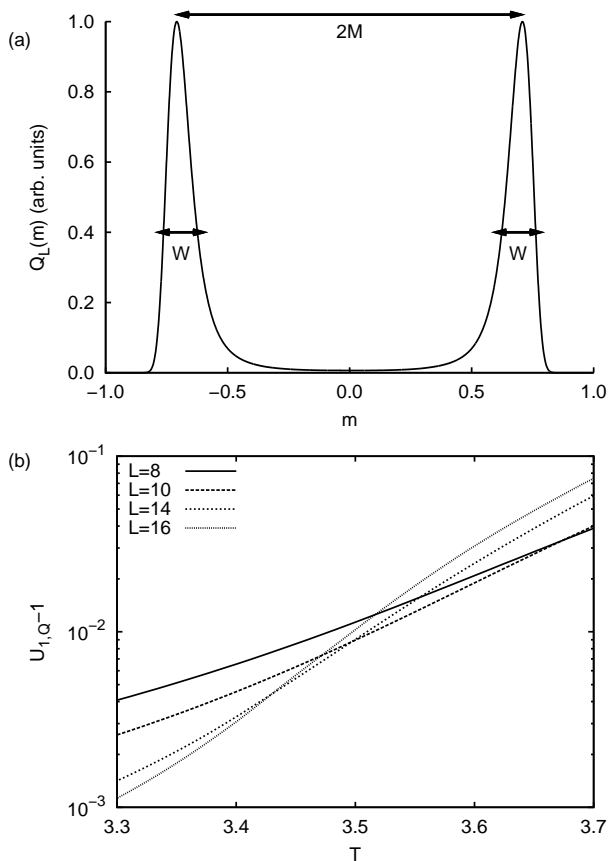


FIG. 7. (a) The quenched-averaged distribution $Q_L(m)$ of the RFIM obtained at $T = T_c^{\text{NB}}$, $L = 14$, and using the symmetry path l_S . The peak-to-peak distance is proportional to the order parameter M , while the peak widths W reflect the sum of thermal and sample-to-sample fluctuations. (b) The leading cumulant of $Q_L(m)$ versus T for various L .

of the individual (normalized) OPDs. Since $P_{L,i}(m)$ is mostly a single peak, located with equal probability at positive or negative values, $Q_L(m)$ is bimodal and symmetric about $m = 0$ (Fig. 7(a)). The peak-to-peak distance corresponds to (twice) the order parameter $M = [|\langle m \rangle|]$, but care is needed to interpret the peak widths W . The moments of $Q_L(m)$ are of the form $[\langle m^k \rangle]$, and so the peak widths correspond to

$$W^2 = [\langle m^2 \rangle] - [|\langle m \rangle|]^2 = \chi_{\text{con}}/L^d + \chi_{\text{dis}}/L^d, \quad (41)$$

which is the sum of thermal fluctuations (set by χ_{con}) and sample-to-sample fluctuations (set by χ_{dis}). Consequently, the leading cumulant of $Q_L(m)$ becomes

$$U_{1,Q} = \frac{[\langle m^2 \rangle]}{[|\langle m \rangle|]^2} = U_{1,\text{dis}} + \frac{\chi_{\text{con}}}{L^d M^2}. \quad (42)$$

Using now the FSS expressions $M \propto L^{-\beta/\nu}$, $\chi_{\text{con}} \propto L^{\gamma/\nu}$, and modified hyperscaling, we obtain

$$U_{1,Q} - U_{1,\text{dis}} \propto L^{-\gamma/\nu} \quad (T = T_c). \quad (43)$$

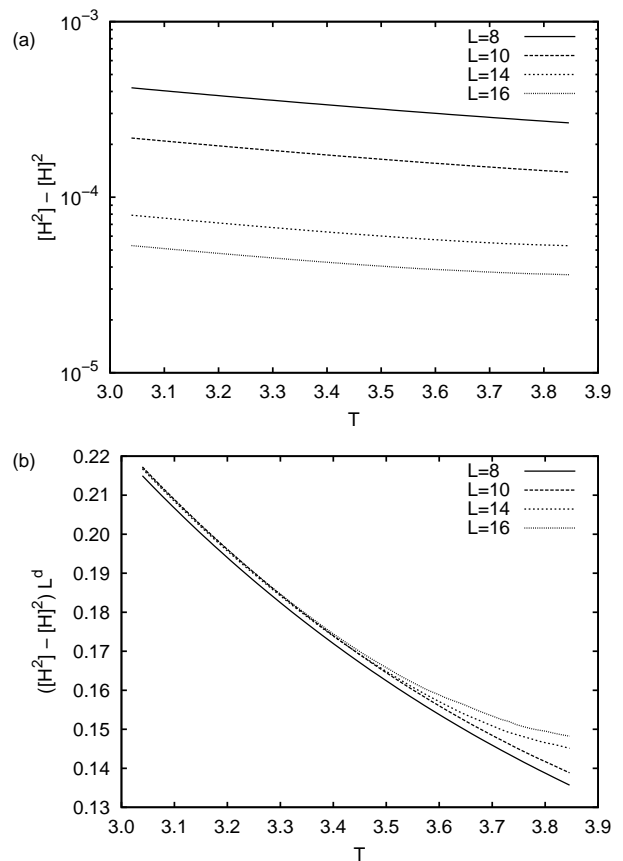


FIG. 8. (a) Variance $[H^2] - [H]^2$ of the “tuned” external fields H_i versus T using the path l_Γ for several system sizes. (b) The variance multiplied by L^d .

Hence, in the thermodynamic limit, $U_{1,Q}$ becomes identical to $U_{1,\text{dis}}$. Plotting $U_{1,Q}$ versus T for different L one therefore also observes intersections (Fig. 7(b)). Note that, due to the correction term induced by the connected susceptibility in Eq. (42), one expects that for small L the intersections are more scattered than those for $U_{1,\text{dis}}$; the data in Fig. 6(b) and Fig. 7(b) are compatible with this expectation.

B. FSS using the path l_Γ

We now use the path l_Γ , where for each random field sample i the external field H_i is tuned according to Eq. (40). We first verify, in Fig. 8, that the variance of H_i indeed decays $\propto 1/L^d$. The raw data are shown in (a), while (b) shows the same data multiplied by L^d . In the latter representation, the L -dependence should cancel for $T \leq T_c$. This is confirmed by the collapse of the data of the larger systems; only the $L = 8$ data is somewhat off, which indicates that this system may be too small for an accurate FSS analysis. The “swaying-out” of the curves at high T is a sign of entering the one-phase

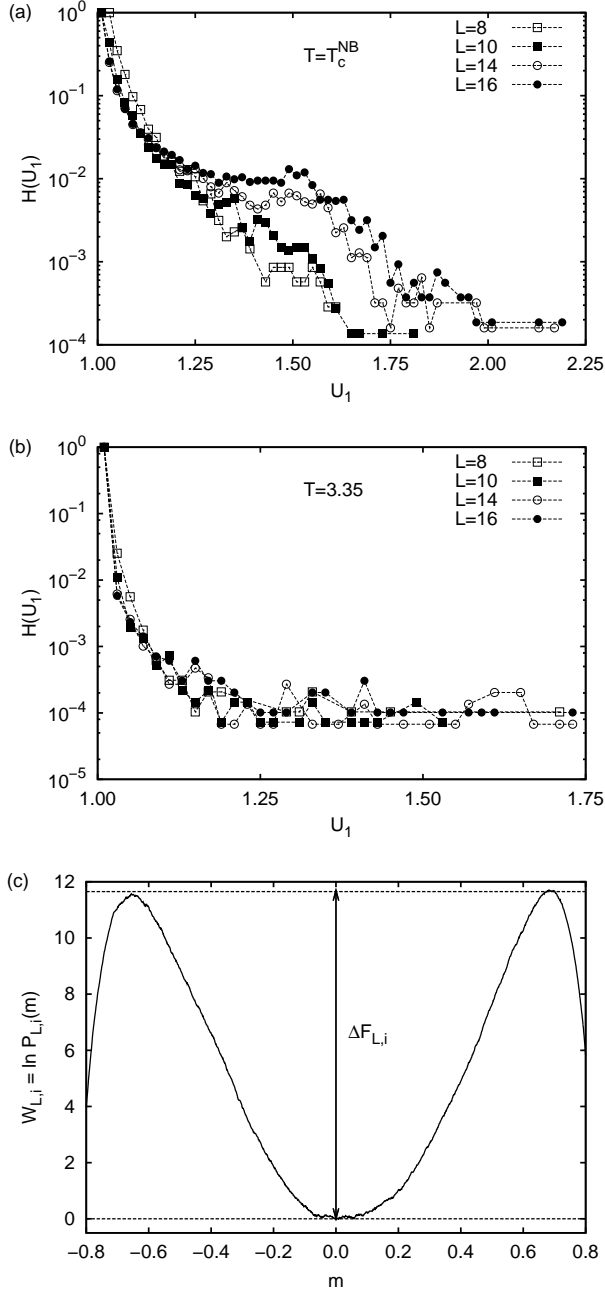


FIG. 9. Investigation of the “typical” shape of $P_{L,i}(m)$ in the RFIM using the path l_{Γ} . Shown are histograms $H(U_1)$ for various L obtained at (a) $T = T_c^{NB}$ and (b) $T = 3.35$. The histograms peak at $U_1 = 1$ implying that most distributions are bimodal. Note the logarithmic vertical scales. (c) Typical distribution $W_{L,i} = \ln P_{L,i}(m)$ obtained for $L = 14$ and $T = T_c^{NB}$. Since $W_{L,i}$ is bimodal, a free energy barrier $\Delta F_{L,i}$ can be extracted (vertical arrow).

region, where the path l_{Γ} becomes ill-defined.

By using l_{Γ} , we expect that most distributions become bimodal for $T \leq T_c$. In Fig. 9, we show histograms of observed cumulant values, for $T = T_c^{NB}$ (a) and $T = 3.35$ (b). We believe the latter temperature is closer to the true T_c , based on the intersections of the disconnected cumulant, Fig. 6(b). The histograms peak at $U_1 = 1$, confirming that bimodal distributions dominate. An example distribution is shown in Fig. 9(c), from which a barrier $\Delta F_{L,i}$ can be accurately extracted (vertical arrow). We remind the reader that the barrier is to be obtained from the logarithm of $P_{L,i}(m)$. Note also an important finite size effect in the histograms $H(U_1)$. At $T = T_c^{NB}$, for increasing L , a shoulder develops at $U_1 \sim \pi/2$, meaning that single-peaked distributions become more likely in larger systems. In contrast, $H(U_1)$ at $T = 3.35$ reveals no such effect. We believe this indicates that $T = T_c^{NB}$ is actually above the critical temperature. Above T_c , in the thermodynamic limit, the OPD is single-peaked. Hence, Fig. 9(a) shows the evolution toward this shape. The convergence with L is clearly very slow, and much larger systems are required before single-peaked distributions would dominate bimodal ones in finite-size simulation data.

The path l_{Γ} facilitates a first test of the scaling of the quenched-averaged barrier $\Delta F_L = (1/K) \sum_{i=1}^K \Delta F_{L,i}$, where the sum is over all K considered random field samples. For distributions where a barrier cannot be meaningfully defined, such as single or triple peaks, $\Delta F_{L,i}$ is set to zero. In Fig. 10(a), we show ΔF_L versus T for various L . Following modified hyperscaling, we expect ΔF_L to scale conform Eq. (39). Hence, plotting $L^{-\theta} \Delta F_L$ versus $tL^{1/\nu}$, $t = T/T_c - 1$, the curves for different L should collapse, provided suitable values of θ , ν , and T_c are used. This result is shown in Fig. 10(b). Here, $\theta = 1.5$ was assumed, and by varying ν and T_c , a data collapse is indeed obtained (the plot uses $\nu = 1.9$ and $T_c = 3.32$). We have verified that by using $\theta = 0$, i.e. the value of the pure model, no data collapse is obtained. The estimate of ν is rather large, but still within the range of values reported in Table I. Note also that T_c used in Fig. 10(b) agrees with that of the disconnected cumulant intersections, Fig. 6(b).

We now propose one additional method to locate the critical temperature. To this end, recall the FSS expressions $\Delta F_L \propto L^{\theta}$ and $\chi_{\text{con}} \propto L^{\gamma/\nu}$. Since $\theta = \gamma/\nu$, the ratio $\kappa = \chi_{\text{con}}/\Delta F_L$ becomes L -independent at criticality. One can thus locate T_c by plotting κ versus T for various system sizes, and look for intersection points. This approach has the advantage that the critical exponents themselves need not be provided. The connected susceptibility is obtained from the individual distributions $P_{L,i}(m)$ using $\chi_{\text{con}} = (L^d/K) \sum_{i=1}^K (\langle m^2 \rangle_i - \langle |m| \rangle_i^2)$. In Fig. 11(a), we plot κ versus T for various L . The data indeed intersect, providing important confirmation that the barrier scales with the same exponent as the connected susceptibility at criticality. For completeness, we show in Fig. 11(b) the disconnected cumulant $U_{1,\text{dis}}$ ver-

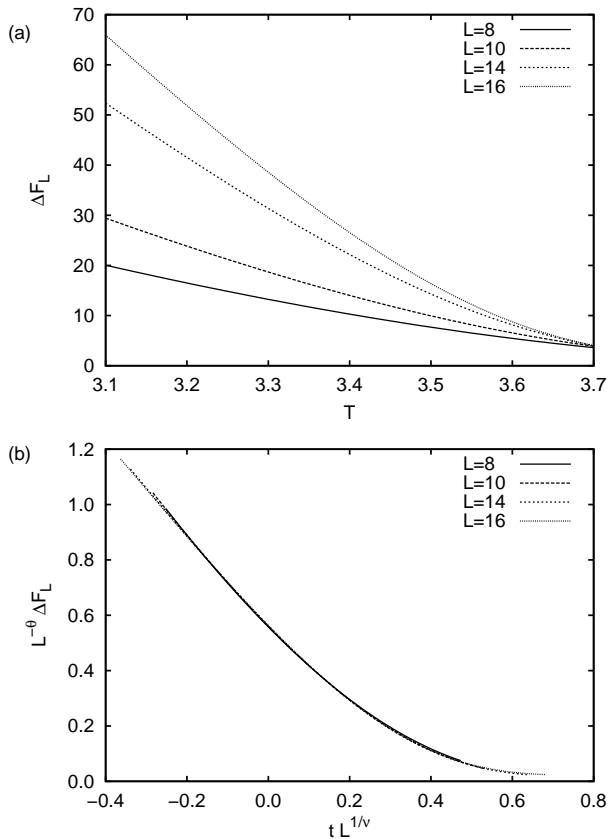


FIG. 10. FSS of the free energy barrier ΔF_L in the RFIM using the path l_Γ . (a) ΔF_L versus T for various system sizes. (b) The same data as in (a) but using scaled variables. The validity of the scaling form, Eq. (39), is confirmed by the collapse of the data from the various system sizes onto a single curve.

sus T for various L (now obtained using the path l_Γ). The curves also intersect, and do so remarkably close to the intersections of κ . Based on Fig. 11, we (VFB) report $T_c^{\text{VFB}} \approx 3.315 \pm 0.050$, where the error reflects the scatter in the various intersection points (here the data of the smallest system $L = 8$ was ignored).

We now turn to the distribution $\mathcal{P}_L(\langle |m| \rangle)$, defined as the probability of a particular random field sample yielding a magnetization $\langle |m| \rangle$. At criticality, we anticipate scaling of this distribution, conform Eq. (36). We have explicitly measured $\mathcal{P}_L(\langle |m| \rangle)$ by accumulating a histogram of $\langle |m| \rangle$ values at $T = T_c^{\text{VFB}}$ using the path l_Γ . The resulting distributions are shown in Fig. 12. The salient features are a sharp peak, and a long tail extending to lower values. The fact that $\mathcal{P}_L(\langle |m| \rangle)$ features a sharp peak is consistent with $U_{1,\text{dis}}$ being close to unity at criticality. Since $\beta \sim 0$ in the RFIM, the scaling variable $x = L^{-\beta/\nu} \langle |m| \rangle$ is identical to $\langle |m| \rangle$ itself, and so the “raw” distributions for different L should already overlap with each other. Within numerical precision this is confirmed, but it is clear that the data in Fig. 12 do not

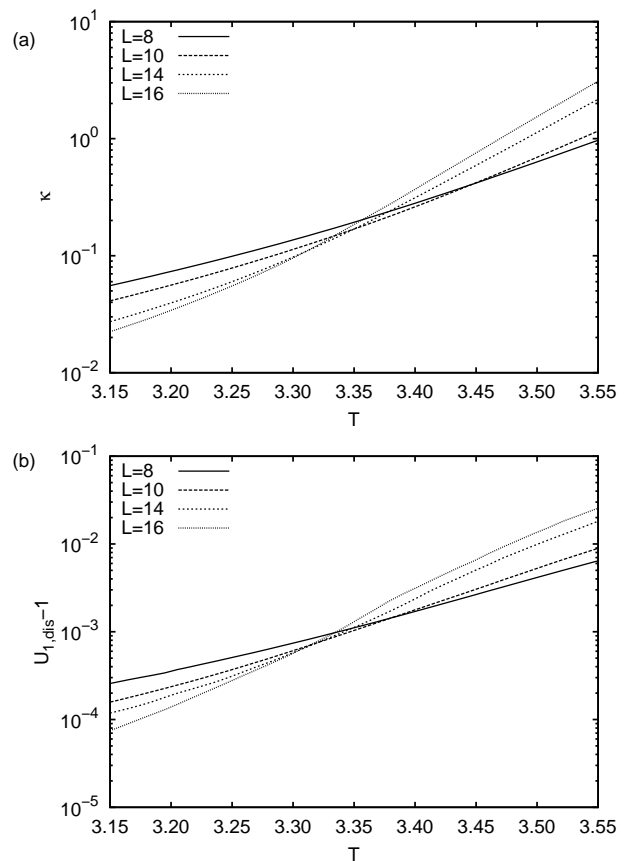


FIG. 11. FSS in the RFIM using the path l_Γ . (a) κ versus T for various L . Note the intersection point, which yields an estimate of T_c . (b) The disconnected cumulant, Eq. (37), versus T for various L . The intersections again yield T_c . For clarity, the cumulant curves are shifted by unity, and a logarithmic vertical scale is used.

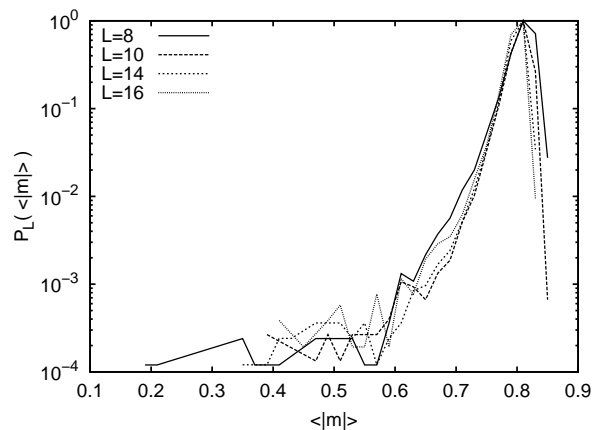


FIG. 12. $\mathcal{P}_L(\langle |m| \rangle)$ for the RFIM at $T = T_c^{\text{VFB}}$, using the path l_Γ , and for various system sizes.

allow for any meaningful estimate of β/ν .

The point that we wish to make, however, is a different one. The fact that $\mathcal{P}_L(\langle|m|\rangle)$ features a long tail means that occasionally a distribution $P_{L,i}(m)$ is observed with a significantly lower magnetization. Since the scaling form, Eq. (36), implies that $\mathcal{P}_L(\langle|m|\rangle)$ retains its shape irrespective of L , the fraction of these distributions does not vanish in the thermodynamic limit. It is conceivable that distributions from the “tail” of $\mathcal{P}_L(\langle|m|\rangle)$ are also shaped differently. For instance, consider again the histogram $H(U_1)$ at T_c (Fig. 9(b)). The histograms peak at $U_1 = 1$, so most distributions $P_{L,i}(m)$ are bimodal. However, $H(U_1)$ also features a tail, so distributions with profoundly different shapes, although rare, do occur. In particular, the tail in $H(U_1)$ allows for three-peaked distributions to be present (for which $U_1 = 3/2$). Indeed, such distributions are observed, and have been interpreted to signify first-order transitions [46], or new phases [47]. Our point is that the long tail of $\mathcal{P}_L(\langle|m|\rangle)$ and its scale invariance at T_c (implied by modified hyperscaling) also allows for the presence of three-peaked distributions (without having to assume a first-order transition, or the emergence of a new phase).

V. WIDOM-ROWLINSON MODEL WITH QUENCHED OBSTACLES

It was argued by de Gennes that a binary mixture undergoing phase separation inside a random network of quenched obstacles belongs to the universality class of the RFIM [48]. The argument is expected to hold when the obstacles display a preferred affinity to one of the phases. In case there is no such preference, the argument does not apply [49, 50]. Previous simulations [6] have already produced evidence in favor of de Gennes’ argument. To provide further confirmation, in particular to test the scaling of the free energy barrier (Eq. (6)), we consider in this section the Widom-Rowlinson binary mixture (WRM) [51]. The model consists of unit diameter spheres, species A or B , which may overlap freely except for a hard-core repulsion between A and B particles. The model is investigated in the grand-canonical ensemble, where the relevant thermodynamic parameters are the fugacities, z_A and z_B , of the respective species.

At high fugacities, the WRM can be in two phases: a phase rich in A particles (the A -phase) when $z_A > z_B$, and a phase rich in B particles (the B -phase) when $z_B > z_A$. Due to the model’s symmetry under the exchange of A and B particles, the phase transition occurs at $z_A = z_B$. Hence, in line with the Ising model, a symmetry path l_S for the WRM can be defined as $l_S : z_A = z_B$. The transition line ends in an Ising critical point, at fugacity $z_A = z_B = z_{\text{crit}}$, below which mixed states appear [52, 53]. Note that the phase transition in the WRM can also be considered a liquid-gas transition. By integrating out the B particles, the WRM maps onto a single component fluid, interacting via a short-ranged

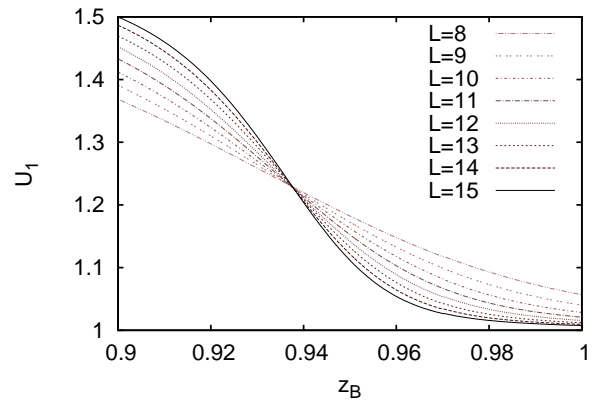


FIG. 13. Cumulant plot for the WRM without quenched disorder. Plotted is U_1 versus z_B for different L . The intersection yields $z_{\text{crit}} = 0.9377(4)$ and $U_1^* = 1.228(5)$.

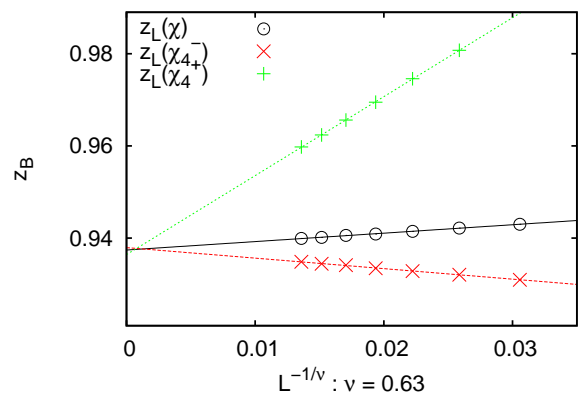


FIG. 14. Extrapolation of $z_L(x)$, $x \in \{\chi, \chi_4^-, \chi_4^+\}$, according to Eq. (45) for the WRM with quenched disorder. From the linear fits $z_{\text{crit}} = 0.9376(5)$ is obtained.

attractive potential [51]. The fugacity z_B then plays the role of inverse temperature, the A -phase corresponds to the liquid (characterized by a high particle density), and the B -phase to a gas (low particle density).

A. pure mixture

We first consider the pure WRM, i.e. without quenched obstacles. We simulate using cubic boxes with periodic boundary conditions (see Appendix 5). The analogue of the Ising model OPD is the distribution $P_L(\rho_A)$, defined as the probability for a system of lateral extension L to contain $N_A = \rho_A L^d$ particles of species A . Since we are ultimately interested in locating the critical point, only OPDs lying on the symmetry path l_S are considered in this section, which leaves z_B as the single free param-

ter. Note that we could also have defined the OPD as $P_L(\rho_A - \rho_B)$, thereby directly exploiting the symmetry of the WRM. However, most fluids lack such an obvious symmetry, and by using $P_L(\rho_A)$ we ensure that our analysis remains generally applicable.

Above the critical fugacity, $z_B > z_{\text{crit}}$, $P_L(\rho_A)$ is bimodal: the peak at low (high) density corresponds to the gas (liquid) phase. When $z_B < z_{\text{crit}}$, the OPD features a single peak, corresponding to a mixed state. The analogue of the magnetization is defined as $m \equiv \rho_A - \langle \rho_A \rangle$, which is readily substituted in Eq. (18) to yield the order parameter and susceptibility. Additionally, we define a “generalized” susceptibility [36, 45]

$$\chi_4 \equiv L^{3d} (\langle m^4 \rangle - 4\langle |m| \rangle \langle |m|^3 \rangle + 12\langle m^2 \rangle \langle |m| \rangle^2 - 3\langle m^2 \rangle^2 - 6\langle |m| \rangle^4). \quad (44)$$

The most straightforward method to locate the critical point is from intersections of the Binder cumulant for different L . For the pure WRM, we find that a sharp intersection of U_1 can be found easily (Fig. 13). Another method to locate the critical fugacity is via the extrapolation of the finite-size extrema of χ and χ_4 . In a finite system of size L , χ reaches a maximum at fugacity $z_L(\chi)$, which is shifted from z_{crit} as [45]

$$z_{\text{crit}} - z_L(\chi) \propto L^{-1/\nu}, \quad (45)$$

with ν the correlation length critical exponent. In addition, χ_4 reaches a minimum and maximum, at respective fugacities $z_L(\chi_4^-)$ and $z_L(\chi_4^+)$, which are also shifted according to Eq. (45). Hence, plotting $z_L(\chi)$, $z_L(\chi_4^-)$, and $z_L(\chi_4^+)$ versus $L^{-1/\nu}$, and then linearly extrapolating to $L \rightarrow \infty$, three additional estimates of z_{crit} are obtained. For this extrapolation, hyperscaling is not required, but ν needs to be provided. In principle, ν can also be taken as a fit parameter, but this requires data of extremely high quality. For the pure WRM, which belongs to the Ising universality class, ν is known (cf. Table I). In Fig. 14, the extrapolation is demonstrated; the resulting estimates of z_{crit} are similar and agree with the cumulant intersections. Combining all results, we obtain $z_{\text{crit}} = 0.9377(5)$, where the error reflects the scatter between the individual estimates. This value is in good agreement with previous results [52, 53].

B. mixture with quenched obstacles

We now consider the WRM model with quenched obstacles. We use spherical obstacles, species X and Y , having the same diameter as the (mobile) A and B particles. The total number of X and Y obstacles equals $N_X = N_Y = \rho_Q \times L^d$, rounded up or down at random to the next integer. The obstacles are distributed randomly at the start of the simulation, irrespective of overlap, after which they remain quenched: this defines one disorder realization i . Next, A and B particles are introduced, and grand canonical MC is used to construct $P_{L,i}(\rho_A)$ for that

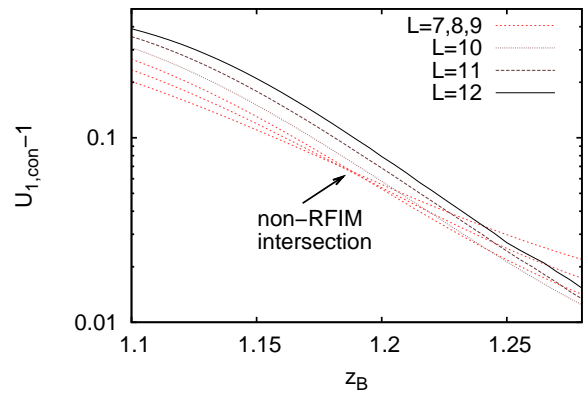


FIG. 15. Cumulant plot for the WRM with quenched obstacles. Plotted is $U_{1,\text{con}}$ (Eq. (35)) versus z_B for different L . The intersection of system sizes $L < 10$ is attributed to a crossover effect from Ising universality to RFIM universality. Curves for $L \geq 10$ no longer intersect at this point indicating that for these system sizes the crossover to RFIM universality has largely completed.

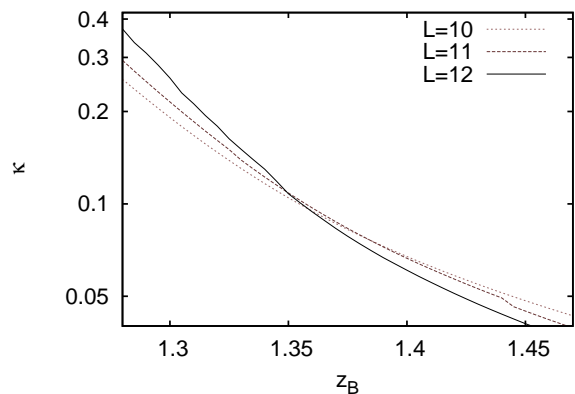


FIG. 16. Variation of κ with z_B for various L for the WRM with quenched obstacles (analogue of Fig. 11(a)). The intersection of the curves indicates a critical point around $z_B \sim 1.35$.

disorder realization (see Appendix). The A -particles (B -particles) have a hard-core interaction with X -obstacles (Y -particles) but do not interact with Y -obstacles (X -obstacles). The original motivation for this choice was to restore the symmetry line $l_S : z_A = z_B$ in the disorder average. However, in what follows, we will use the path l_Γ , whereby z_A is tuned for each realization of disorder such that $\partial \langle \rho_A \rangle / \partial \log z_A$ is maximized.

We still need to specify the obstacle concentration ρ_Q . For a noticeable random field effect, the thermal correlation length ξ should be large compared to the typical distance ξ_Q between obstacles. Following the FSS “Ansatz” $\xi \propto L$, this implies $L \gg \xi_Q$. If L is too small, crossover

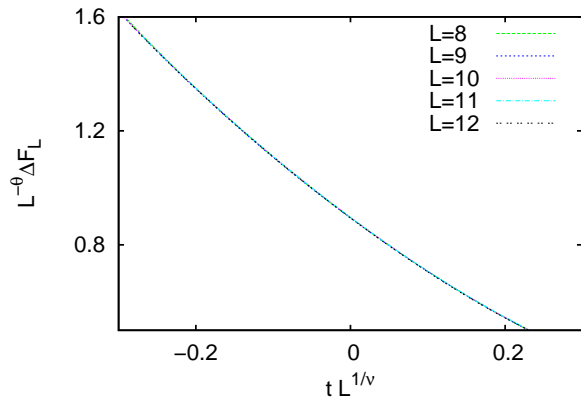


FIG. 17. Scaling plot of the free energy barrier, according to Eq. (39), for the WRM with quenched obstacles (analogue of Fig. 10(b)).

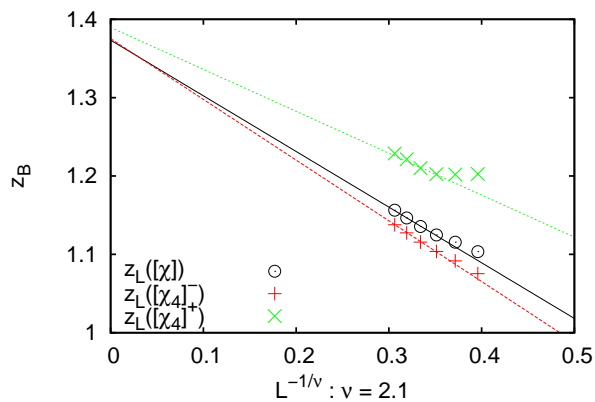


FIG. 18. Extrapolation of $z_L(x)$, $x \in \{[\chi], [\chi_4]^-, [\chi_4]^+\}$, via Eq. (45) for the WRM with quenched disorder. The plot uses $\nu = 2.1$ (as obtained in Fig. 17), and predicts $z_{\text{crit}} = 1.37(2)$ in the limit $L \rightarrow \infty$.

scaling is observed (in this case from pure Ising to random field Ising [6]). From these considerations, choosing a high value of ρ_Q seems optimal. The disadvantage is that also z_{crit} will then be very high, which makes the grand canonical MC approach inefficient due to a high particle density. Clearly, a compromise needs to be made: we use $\rho_Q = 0.02$. This value is small compared to typical density of the mobile species, e.g. $\rho_A = \rho_B \approx 0.38$ at criticality in the pure WRM, and certainly is below the percolation threshold; we thus remain in the limit of weak random fields. For the chosen obstacle density, crossover effects are still strong in small systems. This can be inferred from Fig. 15, where the connected cumulant $U_{1,\text{con}}$ versus z_B for various L is plotted. The curves for $L < 10$ reveal an intersection point: this would be consistent with a conventional critical point featuring standard hyperscaling. However, for $L \geq 10$, the inter-

section has vanished, indicating that the crossover has largely completed. In what follows, we therefore discard the data for $L < 10$ in some of the analysis.

Investigations involving disconnected quantities require enormous simulational effort to generate data of sufficient quality (see Fig. 19 in Appendix 2). For the WRM, an analysis of $U_{1,\text{dis}}$ along the lines of Fig. 11(b) was not feasible. We therefore focus on the free energy barrier. We evaluate the distributions $P_{L,i}(\rho_A)$ along the path l_Γ , and for each distribution, we “read-off” the barrier, which is then averaged over the samples to obtain ΔF_L . We first consider the variation of κ versus z_B for different L , i.e. the analogue of Fig. 11(a). This data is shown in Fig. 16; from the intersection we conclude that the critical fugacity is around $z_B \sim 1.35$. To get the critical exponents, we consider the scaling of the free energy barrier. Assuming RFIM universality, the variation of ΔF_L with z_B should follow Eq. (39), where now $t \equiv (z_{\text{crit}} - z_B)/z_B$. In the vicinity of $z_B \sim 1.35$, i.e. as indicated by Fig. 16, we indeed find that a collapse of the curves can be realized for $\theta = 1.32$, $\nu = 2.1$, and $z_{\text{crit}} = 1.37$ (Fig. 17). As a consistency check, we attempt to obtain z_{crit} from the extrapolation of the extrema of the susceptibilities using Eq. (45). The observables χ and χ_4 of the pure model are now replaced by their disorder-averaged counterparts $[\chi]$ and $[\chi_4]$, and $\nu = 2.1$, i.e. the estimate from Fig. 17, is used. The extrapolation works reasonably well (Fig. 18) and for the critical fugacity we obtain the same estimate as before: $z_{\text{crit}} = 1.37(2)$.

VI. SUMMARY

Modified hyperscaling, Eq. (2), which is believed to describe systems belonging to the universality class of the RFIM, gives rise to rather unusual finite size effects at critical points: neither the order parameter distribution, nor the free energy barrier ΔF_L of interface formation, are scale invariant. As a result, “standard” techniques to locate critical points, such as the “cumulant intersection method” [14], or the Lee-Kosterlitz method [43], break down. However, by carefully considering the consequences of Eq. (2), alternative techniques to derive T_c in random field systems can be derived. In this paper, we have proposed two such techniques. The first is based on the order parameter fluctuations between disorder samples: modified hyperscaling predicts that these are scale invariant at T_c . This property can be used to locate T_c by measuring the *disconnected* cumulant $U_{1,\text{dis}}$ (Eq. (37)) versus temperature for various system sizes: at T_c , curves for different L intersect. Indeed, simulation data of the RFIM confirm the scaling of $U_{1,\text{dis}}$ (Fig. 6(b) and Fig. 11(b)). In contrast to conventional critical points, there is no intersection of the *connected* cumulant $U_{1,\text{con}}$ (Eq. (35)) in the RFIM at T_c . However, in small systems, there may be crossover effects. In this case, an apparent intersection in $U_{1,\text{con}}$ is observed, at $T > T_c$, but it vanishes in larger systems; such was the

case for the WRM (Fig. 15).

The practical disadvantage of measuring $U_{1,\text{dis}}$ is that many disorder samples must be averaged over if meaningful results are to be obtained. Particularly for more complex systems, such as *off-lattice* fluids, an economic alternative is to consider the free energy barrier ΔF_L of interface formation. Due to modified hyperscaling, the barrier diverges $\Delta F_L \propto L^\theta$ at T_c , with θ the violation of hyperscaling exponent. The consequences of this divergence are easily detected in simulations, as was demonstrated for the RFIM (Fig. 10 and Fig. 11(a)), and the WRM (Fig. 16 and Fig. 17). In case of the RFIM, the estimate of T_c obtained from the scaling of the barrier was fully consistent with that obtained from the intersections of $U_{1,\text{dis}}$ (Fig. 11). Our results for the WRM provide further confirmation that fluids with quenched disorder indeed belong to the universality class of the RFIM, consistent with the conjecture of de Gennes [48].

We have also commented on the variations in shape of the order parameter distribution between samples. There is some question as to whether distributions with three peaks signify first-order transitions [46], or the emergence of new phases [47]. Our view is that modified hyperscaling also allows for these shape variations. While our data indicate that at T_c , and using the path l_Γ , the majority of distributions is bimodal, a fraction of distributions with different shape is not ruled out (Fig. 9(b) and Fig. 12).

Finally, we remind the reader that the divergence of the free energy barrier at T_c will also influence the dynamics. Taking the RFIM with single spin-flip dynamics as example, it follows that the largest relaxation time in a finite system at criticality is given by an Arrhenius' type formula

$$\ln \tau \propto L^\theta \quad (T = T_c). \quad (46)$$

This is in contrast to the pure model, where the relaxation time (not its logarithm) scales $\tau \propto L^z$, with z the "dynamical critical exponent". Such a power law for the logarithm of the relaxation time is the hallmark of "activated critical dynamics". In fact, if we are somewhat above T_c , but the system size is still less than the correlation length, $L < \xi$, Eq. (46) still holds! As $L > \xi$, the system size in Eq. (46) gets replaced by ξ , and we recover Eq. (4), as proposed by Villain [25] and Fisher [26]. A direct study of the dynamics of a kinetic version of the RFIM would be illuminating, but goes beyond the scope of the present paper.

ACKNOWLEDGMENTS

This work was supported by the *Deutsche Forschungsgemeinschaft* (Emmy Noether program: VI 483/1-1).

-
- [1] Y. Imry and S. K. Ma, Phys. Rev. Lett. **35**, 1399 (1975)
 - [2] S.F. Edwards and P.W. Anderson, J. Phys. F **5**, 965 (1975)
 - [3] R.B. Stinchcombe, *Dilute Magnetism*, in: Phase Transitions and Critical Phenomena, Vol 7, edited by C. Domb and J.L. Lebowitz (Academic Press, London, 1983) p. 151.
 - [4] A.P. Young (ed.) *Spin Glasses and Random Fields* (World Scientific, Singapore, 1998)
 - [5] K. Binder and W. Kob, *Glassy Materials and Disordered Solids: An Introduction to their Statistical Mechanics* (World Scientific, Singapore, 2005)
 - [6] R.L.C. Vink, K. Binder and H. Löwen, Phys. Rev. Lett. **97**, 230603 (2006); J. Phys.: Condens. Matter **20**, 404222 (2008)
 - [7] M. E. Fisher, Rev. Mod. Phys. **46**, 597 (1974)
 - [8] J. Zinn-Justin, Phys. Rep. **344**, 159 (2001)
 - [9] K. Binder, Rep. Progr. Phys. **60**, 487 (1997)
 - [10] K. Binder and E. Luijten, Phys. Rep. **344**, 179 (2001)
 - [11] K. Binder and D. W. Heermann, *Monte Carlo Simulation in Statistical Physics. An Introduction*, 4th Ed. (Springer, Berlin, 2002)
 - [12] M. E. Fisher, in *Critical Phenomena*, ed. by M.S. Green (Academic Press, London, 1971) p.1.
 - [13] V. Privman (ed.) *Finite Size Scaling and Numerical Simulation of Statistical Systems* (World Scientific, Singapore, 1990)
 - [14] K. Binder, Z. Phys. B **43**, 119 (1981)
 - [15] K. Binder, Phys. Rev. A **25**, 1699 (1982)
 - [16] K. Binder and D.P. Landau, Phys. Rev. B **30**, 1477 (1984)
 - [17] A. Aharony and A. B. Harris, Phys. Rev. Lett. **77**, 3700 (1996)
 - [18] S. Wiseman and E. Domany, Phys. Rev. Lett. **81**, 22 (1998); Phys. Rev. E **52**, 3469 (1995); Phys. Rev. E **58**, 2938 (1998)
 - [19] E. Kierlik, P. A. Monson, M. I. Rosinberg, and G. Tarjus, J. Phys.: Condens. Matter **14**, 9295 (2002)
 - [20] A. Malakis and N. G. Fytas, Phys. Rev. E **73**, 016109 (2006)
 - [21] P.E. Berche, C. Chatelain, B. Berche and W. Janke, Eur. Phys. J. B **38**, 463 (2004)
 - [22] J.Z. Imbrie, Phys. Rev. Lett. **53**, 1747 (1984)
 - [23] H. Rieger, Phys. Rev. B **52**, 6659 (1995)
 - [24] M. E. J. Newman and G. T. Barkema, Phys. Rev. E **53**, 393 (1996)
 - [25] J. Villain, J. Phys. (France) **46**, 1843 (1985)
 - [26] D. S. Fisher, Phys. Rev. Lett. **56**, 416 (1986)
 - [27] T. Nattermann, *Theory of the Random Field Ising Model*, in: *Spin Glasses and Random Fields*, edited by A. P. Young (World Scientific, Singapore, 1998), p. 277; see also arXiv:cond-mat/9705295
 - [28] M. Schwartz, J. Phys. C: Solid State Phys. **18**, 135 (1985)
 - [29] M. Schwartz, M. Gofman, and T. Nattermann, Physica A **178**, 6 (1991)
 - [30] M. Gofman, J. Adler, A. Aharony, A.B. Harris, and M. Schwartz, Phys. Rev. Lett. **71**, 1569 (1993)
 - [31] P.C. Hohenberg and B.I. Halperin, Rev. Mod. Phys. **49**, 435 (1977)

- [32] A.P. Young and M. Nauenberg, Phys. Rev. Lett. **54**, 2429 (1985)
- [33] E. Eichhorn and K. Binder, Europhys. Lett. **30**, 331 (1995); J. Phys.: Condens. Matter **8**, 5209 (1996)
- [34] H. E. Stanley, *Introduction to Phase Transitions and Critical Phenomena* (Oxford University Press, Oxford, 1971)
- [35] N. G. Fytas, A. Malakis, and K. Eftaxias, J. Stat. Mech. **2008**, P03015 (2008)
- [36] G. Orkoulas, A. Z. Panagiotopoulos, and M. E. Fisher, Phys. Rev. E **61**, 5930 (2000)
- [37] A. K. Hartmann and U. Nowak, Eur. Phys. J. B **7**, 105 (1999)
- [38] M. S. Cao and J. Machta, Phys. Rev. B **48**, 3177 (1993)
- [39] C. Borgs and R. Kotecký, J. Stat. Phys. **61**, 79 (1990)
- [40] N. B. Wilding and A. D. Bruce, J. Phys. Condens. Matter. **4**, 3087 (1992)
- [41] E. Luijten, M. E. Fisher, and A. Panagiotopoulos, Phys. Rev. Lett. **88**, 185701 (2002)
- [42] B. Grossmann and M. L. Laursen, Nucl. Phys. B, **408** 637 (1993)
- [43] J. Lee and J. M. Kosterlitz, Phys. Rev. Lett. **65**, 137 (1990)
- [44] C. Borgs and S. Kappler, Phys. Lett. A **171**, 37 (1992)
- [45] G. Orkoulas, M. E. Fisher, and A. Z. Panagiotopoulos, Phys. Rev. E **63**, 051507 (2001)
- [46] J. Machta, M. E. J. Newman, and L. B. Chayes, Phys. Rev. E **62**, 8782 (2000)
- [47] M. Álvarez, D. Levesque, and J.-J. Weis, Phys. Rev. E **60**, 5495 (1999)
- [48] P. G. de Gennes, J. Phys. Chem. **88**, 6469 (1984)
- [49] P. G. De Sanctis Lucentini and G. Pellicane, Phys. Rev. Lett. **101**, 246101 (2008)
- [50] R.L.C. Vink, Soft Matter **5**, 4388 (2009)
- [51] B. Widom, J. S. Rowlinson, J. Chem. Phys. **52**, 1670 (1970).
- [52] G. Johnson, H. Gould, J. Machta, L.K. Chayes, Phys. Rev. Lett. **79**, 2612 (1997).
- [53] R.L.C. Vink, J. Chem. Phys. **124**, 094502 (2006)
- [54] F. Wang and D. P. Landau, Phys. Rev. Lett. **86**, 2050 (2001)
- [55] A. M. Ferrenberg and R. H. Swendsen, Phys. Rev. Lett. **61**, 2635 (1988)
- [56] P. Virnau and M. Müller, J. Chem. Phys. **120**, 10925 (2004)

Appendix: Simulation Details

1. Wang-Landau sampling

The simulations of the Ising and RFIM were performed using Wang-Landau (WL) sampling [54]. The OPD is written as

$$P_{L,i}(S) \propto g_{L,i}(S)e^{HS/k_B T}, \quad (\text{A.1})$$

with $S = L^d m$ the total instantaneous magnetization, and $g_{L,i}(S)$ some generalized density of states (DOS). Note that the DOS depends on system size L , temperature T , and random field sample i , but not on the external field H (for the pure Ising model, there is no dependence

on i either, of course). At the start of each simulation, we generate a sample of random fields i . We then perform single spin-flips, whereby one of the spins is chosen at random, and its orientation reversed. Let the total magnetization and energy at the start of each spin-flip be given by S_0 and E_0 , respectively, and afterward by S_1 and E_1 ; each spin-flip is then accepted with probability

$$a(S_0, E_0 \rightarrow S_1, E_1) = \min \left[1, \frac{g_{L,i}(S_0)}{g_{L,i}(S_1)} e^{-(E_1 - E_0)/k_B T} \right]. \quad (\text{A.2})$$

Note that the energy above refers to the configurational part of the Hamiltonian only, i.e. the nearest-neighbor interaction and the coupling to the random field, but not the coupling to the external field.

The DOS is *a-priori* unknown, and is initially set to unity $g_{L,i}(S) = 1$. After each attempted spin-flip, one “updates” the DOS $g_{L,i}(S) \rightarrow f \times g_{L,i}(S)$, with S the magnetization of the system after the attempted spin-flip. The update is performed irrespective of whether the spin-flip was accepted; the initial modification factor $f = e \approx 2.72$. We also update a histogram $h(S) \rightarrow h(S) + 1$, counting how often a state with magnetization S was visited. This procedure is repeated until $h(S)$ has become sufficiently flat, which completes one WL iteration. We use the criterion $(h_{\max} - h_{\min}) / (h_{\max} + h_{\min}) < 10^{-5}$, with h_{\min} and h_{\max} the smallest and largest entries in $h(S)$, respectively. After the first WL iteration, the modification factor is reduced $f \rightarrow f^{1/2}$, the histogram $h(S)$ is reset to zero, and the procedure is repeated. WL iterations are continued until f has become small such that changes to the DOS become negligible. For each DOS, we typically performed 150–250 WL iterations. Once the DOS is known, the OPD can be calculated for arbitrary values of H using Eq. (A.1).

2. Importance of disorder averaging

To accurately determine disorder averages, the OPD $P_{L,i}(m)$ is measured $i = 1, \dots, K$ times. In particular disconnected quantities require a large number of disorder samples if meaningful results in the critical regime are to be obtained. Fig. 19 shows a typical “running average” of χ_{con} and χ_{dis} versus K . While χ_{con} saturates to a plateau already after 1000 samples, the convergence of χ_{dis} is noticeably slower. The data of Fig. 19 indicate that K should exceed several thousands at least. Away from the critical point, χ_{dis} is no longer divergent, and here we expect that lower values of K will also suffice.

3. Histogram reweighting in temperature

A key ingredient in this work is the use of histogram reweighting in the temperature-like variable. We perform our simulations at only a few distinct temperatures, and

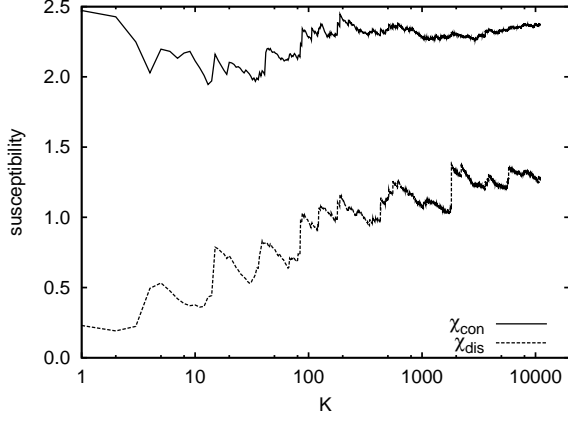


FIG. 19. “Running averages” of the connected and the disconnected susceptibility versus the number of random field samples K . The data were obtained for the RFIM using the symmetry path l_S , $L = 14$, and $T = T_c^{\text{VFB}}$. Note the logarithmic horizontal scale.

extrapolate to other values using histogram reweighting [55]. This requires that the joint two-dimensional probability distribution $P_{L,i}(S, E)$, of the magnetization S and energy E , is known. Again, as in Eq. (A.2), E refers to the configurational part of the Hamiltonian only. If $P_{L,i}(S, E)$ is measured for $T = T_0$ and $H = H_0$, it can be extrapolated to other values using a generalization of Eq. (A.1)

$$P_{L,i}(S, E)|_{T_1, H_1} \propto P_{L,i}(S, E)|_{T_0, H_0} \times e^{\delta h S - \delta \beta E}, \quad (\text{A.3})$$

with $\delta h = (H_1 - H_0)/k_B T_1$ and $\delta \beta = 1/k_B T_1 - 1/k_B T_0$. The practical problem is that two-dimensional histograms require considerable disk space, which in the case of quenched disorder is multiplied by a factor K . Fortunately, an excellent approximation can be used to drastically reduce storage requirements [6]. Without loss of generality, we write

$$P_{L,i}(S, E) = P_{L,i}(S) \times g_{L,i}^{(S)}(E), \quad (\text{A.4})$$

where $g_{L,i}^{(S)}(E)$ is the probability distribution of the energy measured at states with the same magnetization S . The approximation is to assume that $g_{L,i}^{(S)}(E)$ is Gaussian, and so is fully specified by its first two moments. For each random field sample, the two-dimensional histogram of Eq. (A.4) then requires only $P_{L,i}(S)$ to be stored, plus the “functions” $\langle E \rangle_{L,i}(S)$ and $\langle E^2 \rangle_{L,i}(S)$.

4. Alternative method to measure the barrier

It is also possible to measure the quenched-averaged free energy barrier ΔF_L using the same external field for all samples. To be concrete, consider the OPD $P_{L,i}(S)$ of the RFIM obtained at fixed $H = 0$, i.e. the symmetry

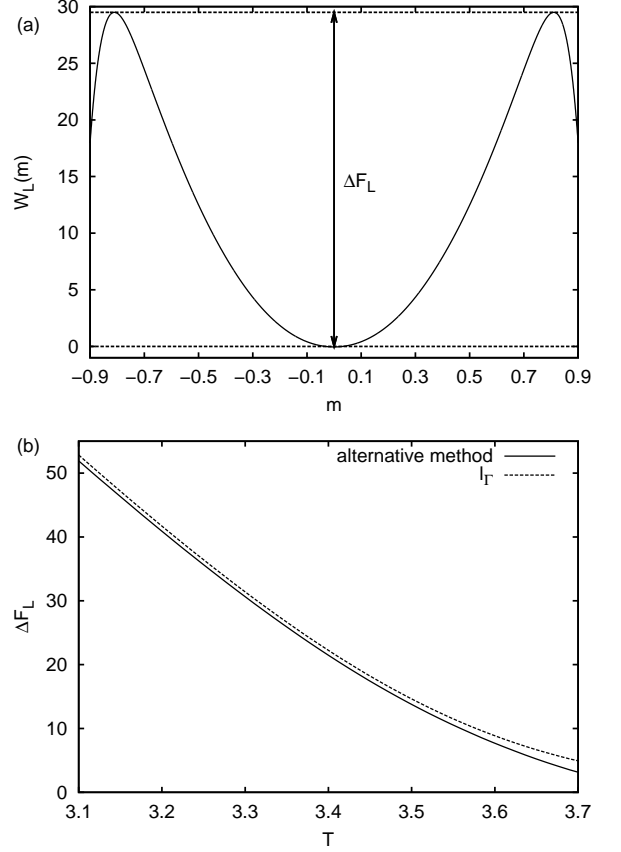


FIG. 20. Demonstration of an alternative method to extract the free energy barrier ΔF_L . The data in this figure were obtained for the RFIM using $L = 14$. (a) The quenched-averaged free energy distribution $W_L(m)$ constructed with the recursion relation of Eq. (A.6) at $T = T_c^{\text{VFB}}$; a free energy barrier ΔF_L can be meaningfully extracted. (b) The corresponding variation of ΔF_L versus T , compared to the “original” method, where ΔF_L is averaged over individual samples using the path l_Γ .

path, with total magnetization $S = -L^d, -L^d + 2, \dots, L^d$ and $i = 1, \dots, K$. We define the quenched-averaged free energy difference between “adjacent” states as

$$\Delta W_L(S-2, S) = \frac{1}{K} \sum_{i=1}^K \ln \left(\frac{P_{L,i}(S)}{P_{L,i}(S-2)} \right), \quad (\text{A.5})$$

which can be used to construct a total free energy $W_L(S)$ by means of recursion

$$\begin{aligned} W_L(-L^d) &\equiv 0, \\ W_L(S) &= W_L(S-2) + \Delta W_L(S-2, S). \end{aligned} \quad (\text{A.6})$$

Fig. 20(a) shows the typical shape of the free energy obtained in this way for the RFIM. The distribution is bimodal, and a free energy barrier ΔF_L can be meaningfully “read-off”. As it turns out, this barrier is very similar to that obtained by averaging over individual samples,

i.e. as was done in Fig. 10(a) using the path l_Γ ; a comparison is provided in Fig. 20(b). In fact, if one uses $W_L(S)$ to perform the scaling analysis of Fig. 10(b), excellent data collapses are also realized.

An analysis in terms of $W_L(S)$ is numerically convenient because extrapolations in the field variable H can be performed after the quenched average has been taken

$$W_L(S)|_{H_1} = W_L(S)|_{H_0} + (H_1 - H_0)S/k_B T. \quad (\text{A.7})$$

This is particularly useful for fluids, where the critical field (chemical potential) is generally not known beforehand. However, it is not obvious what the peak positions and widths in $W_L(S)$ correspond to. Based on our previous work [6], cumulants of $e^{W_L(S)}$ do intersect at T_c , but (in hindsight) we believe it is safer to perform the cumulant analysis using the individual OPDs (as was done in this work).

5. Simulating the Widom-Rowlinson model

We measure $P_{L,i}(\rho_A)$ using grand canonical MC and successive umbrella sampling (SUS) [56]. The simulations are performed in a periodic 3D cube of volume $V = L^3$. At the start of each simulation, a disorder realization i is generated by distributing the obstacles X and Y randomly in the cube, i.e. the obstacles are allowed to overlap. We then perform grand canonical MC moves consisting of the insertion and removal of single A and B particles. In SUS, the full density range of interest is split into overlapping windows W_k . In the first window, N_A is allowed to fluctuate between 0 and 1, in the second window between 1 and 2, or, more generally, in the k -th window $W_k : N_A \in \{k, k+1\}$. There is no restriction on the number of B particles: N_B thus fluctuates freely in each window.

For $N_A = 0$ the B -particles are an ideal gas in the volume allowed by the quenched Y -particles so an initial state for W_0 is easily constructed: we draw a number N from a Poissonian distribution $P(N) = e^{-z_B V} (z_B V)^N / N!$, and randomly insert this number of B -particles into the system, discarding all B -particles that overlap with Y -obstacles. As starting state for the subsequent windows W_k ($k > 0$), we take the last state of the window W_{k-1} preceding it, and equilibrate this state briefly for $\sim 10^5$ MC steps within the bounds of the new window. This works well in practice because the windows are small.

The production run of each window W_k is performed using $\sim 10^7$ MC steps. Each step first selects a species, $x \in \{A, B\}$, with equal probability. Then, with equal probability, the insertion or removal of a particle of species x is attempted. In case of removal, a particle of species x is picked at random and removed from the system; the resulting new state is accepted with probability

$$a(N_x \rightarrow N_x - 1) = \min \left[1, \frac{N_x}{z_x V} f_k^{-1} \right]. \quad (\text{A.8})$$

The factor f_k is one when $x = B$; for $x = A$, it will be specified later. In case insertion is chosen, a new particle

of species x is placed at a random location; the resulting new state is accepted with probability

$$a(N_x \rightarrow N_x + 1) = \min \left[1, \frac{z_x V}{N_x + 1} f_k \right]. \quad (\text{A.9})$$

States with hard-core overlaps and states where N_A is outside the window bounds are always rejected, irrespective of the accept probabilities.

While simulating in window W_k , we keep track of two counters, C_k^- and C_k^+ . These count, respectively, how often the state with $N_A = k$ and $N_A = k+1$ was visited. From these counters, we construct the relative probability of these states via

$$\frac{P_{L,i}(k+1)}{P_{L,i}(k)} \approx \frac{C_k^+}{C_k^-} f_k^{-1}. \quad (\text{A.10})$$

Having at hand this ratio for all windows W_k , the full distribution is constructed recursively

$$P_{L,i}(N_A) \propto \prod_{k=0}^{N_A-1} \frac{P_{L,i}(k+1)}{P_{L,i}(k)} \approx \prod_{k=0}^{N_A-1} \frac{C_k^+}{C_k^-} f_k^{-1}, \quad (\text{A.11})$$

where the proportionality constant follows from normalization. Note that $P_{L,i}(N_A)$ above is, of course, fully equivalent to the OPD $P_{L,i}(\rho_A)$ that we wish to find.

We now specify the factor f_k for moves involving A -particles. Assuming a constant number of steps per window, Eq. (A.10) suggests that optimal results are obtained when f_k is chosen such that C_k^+ and C_k^- are roughly equal, i.e. $f_k = P_{L,i}(k)/P_{L,i}(k+1)$, which is the sought-for result itself. For the first window $k=0$ we use the pure model's optimal weight, which can be calculated analytically. For the subsequent windows, we linearly extrapolate $P_{L,i}(N_A)$ to calculate $f_k = P_{L,i}(k-1)/P_{L,i}(k)$ to be used in that window. In practice, this choice is already quite good, and the counts in the upper and lower bin consistently lie within 1% of each other.

In view of the huge amount of disorder realizations required, a mechanism that allows for histogram reweighting of results obtained at (z_A, z_B) to nearby parameters (\bar{z}_A, \bar{z}_B) is indispensable. To facilitate this reweighting, the joint probability distribution $P_{L,i}(N_A, N_B)$ is stored in compact form as described in Appendix 3; the results of that section trivially transfer to the WRM if one identifies $S \leftrightarrow N_A$ and $E \leftrightarrow N_B$. For the WRM with quenched disorder, the range in z_B over which one can reliably extrapolate is too small to cover the full region of interest. In particular, simulation data obtained at the fugacity $z_L([\chi])$ of the susceptibility maximum could not be extrapolated to the critical fugacity z_{crit} . We therefore created two data sets per system size. One set with $K = 2000$ disorder realizations at $z_B \approx z_L([\chi])$ used for locating the extrema of χ and χ_4 (Fig. 18) and one set with $K = 10000$ realizations around $z_B \approx 1.4$, which is close to z_{crit} , for investigating the free energy barrier (Figs. 16 and 17).